ROYAL SOCIETY
OF CHEMISTRY

PAPER

Check for updates

Bridging structure and dynamics: mechanistic insights into CMK-3 incorporated amide–hydride composite systems for solid-state hydrogen storage

Mohsin Abbas,[a] Fahim Karimi,*[a] Thi Thu Le,[a] Jacques Ollivier,[b] Jitendra Mata,[cd] Joshua P. King,[c] Lathapriya Vellingiri,[a] Gerd Stahlkopf, [ID][a] Thomas Klassen[ae] and Claudio Pistidda [ID] *[a]

The influence of ordered mesoporous carbon (CMK-3) on the hydrogen storage properties of the $6Mg(NH_2)_2-9LiH-2LiBH_4$ reactive hydride composite (6:9:2-RHC) is systematically investigated. Incorporation of 10 wt% CMK-3 into the pristine composite (6:9:2-RHC + 0.1CMK3) leads to substantial improvements in hydrogen sorption kinetics. Under identical thermodynamic conditions, the CMK-3 incorporated composite exhibits significantly enhanced reaction kinetics, with the absorption time reduced from ∼30 minutes to only 3 minutes (≈90% improvement) and the full desorption completed within 25 minutes instead of 60 minutes (≈58% improvement) compared to the pristine system. Moreover, the modified composite maintains excellent cycling stability, with 98% capacity retention over the first ten dehydrogenation/hydrogenation cycles compared to 90% for the pure composite. To elucidate the mechanism underlying this kinetic enhancement, we use a combination of advanced characterization techniques, including differential thermal analysis (DTA), synchrotron radiation X-ray powder diffraction (SR-XRPD), Fourier transform infrared (FT-IR) spectroscopy, small-angle and ultra-small-angle neutron scattering (SANS/USANS) and quasi-elastic neutron scattering (QENS). DTA analysis shows an 11 kJ mol^{-1} decrease in apparent activation energy barrier upon CMK-3 addition. SANS/USANS results reveal that CMK-3 effectively suppresses particle agglomeration during the dehydrogenation/hydrogenation cycle and maintains structural integrity, preserving the high accessible surface area for long-term cycling stability. QENS measurements confirm that the incorporation of mesoporous carbon lowers the reorientational energy barriers of $[BH_4]^-$ anions, leading to faster local dynamics. This enhanced mobility facilitates the elementary reaction steps involved in hydrogen release and uptake, which contributes to the improved sorption kinetics of the CMK-3 modified composite.

1. Introduction

Efficient and safe hydrogen storage remains a key challenge in the implementation of hydrogen-based energy systems.[1–3] Among various storage approaches, solid-state hydrogen storage in complex metal hydrides offers distinct advantages in safety, volumetric energy density and reversibility, making it a significant research focus over the past few decades.[4–6]

[a]Institute of Hydrogen Technology, Helmholtz-Zentrum Hereon, Geesthacht, 21502, Germany. E-mail: fahim.karimi@hereon.de; claudio.pistidda@hereon.de

[b]Institut Laue-Langevin, 71 Avenue des Martyrs, CS 20156, 38042 Grenoble Cedex 9, France

[c]Australian Centre for Neutron Scattering, ANSTO, New Illawarra Rd, Lucas Heights, 2234, NSW, Australia

[d]School of Chemistry, University of New South Wales, Sydney 2052, Australia

[e]Helmut Schmidt University, University of the Federal Armed Forces Hamburg, Hamburg, 22043, Germany

Complex metal hydrides such as alanates $[AlH_4]^-$, borohydrides $[BH_4]^-$ and amides $[NH_2]^-$ (ref. 7–16) have been extensively investigated due to their higher hydrogen storage capacities (5–15 wt%) and tunable thermodynamic and kinetic properties.[5,17] Amides were initially disregarded as hydrogen storage materials due to ammonia emission during their thermal decomposition.[18] Chen *et al.* (2002) was the first to demonstrate reversible hydrogen storage in $LiNH_2$ by the addition of LiH, which stabilized the desorption product and suppressed NH_3 formation.[19] This sparked a renewed interest in the metal–N–H based materials for solid-state hydrogen storage.

Since then, various metal–N–H based systems have been developed to enhance hydrogen storage performance.[20–25] Among them, the $Mg(NH_2)_2-2LiH$ composite has attracted considerable attention due to its favorable thermodynamics, relatively high hydrogen storage capacity (5.5 wt% H_2) and excellent reversibility.[26–28] The dehydrogenation enthalpy of 40

kJ mol^{-1} H$_2$ corresponds to an equilibrium temperature near 90 °C at 1 bar H$_2$ pressure, and this thermodynamics is suitable for practical applications. However, the system suffers from sluggish kinetics due to a high activation energy barrier and requires temperatures above 180 °C to complete dehydrogenation within one hour. Many efforts have been made to improve both the thermodynamics and kinetics of hydrogen storage in the Mg(NH$_2$)$_2$–2LiH system.[29–32]

Kinetic improvements of the Mg(NH$_2$)$_2$–2LiH system have been achieved through the introduction of additives such as Ru/C-, Rb-, K- and Ca-based compounds. These additives not only act as catalytic species but also destabilize the reactants, lowering the activation energy of the hydrogen storage reactions and thereby accelerating the overall reaction kinetics.[33–37] Thermodynamic improvement of Mg(NH$_2$)$_2$–LiH was achieved by the addition of LiI, LiBr and LiBH$_4$, which reduced the dehydrogenation enthalpy of the composite system from 40 kJ mol^{-1} H$_2$ to 33 kJ mol^{-1} H$_2$, 32 kJ mol^{-1} H$_2$ and 36 kJ mol^{-1} H$_2$, respectively. However, the composite system with LiBH$_4$ shows faster reaction kinetics and higher hydrogen storage capacity in comparison to the lithium halide additives.[38–40] Yang *et al.* attributed this enhanced reaction kinetics and improved hydrogen capacity to the *in situ* formation of Li$_4$BH$_3$H$_{10}$ solid-solution, which promotes faster mass transport and facilitates a reversible hydrogen exchange process through ancillary reactions.[41,42] Building on these developments, previous research efforts at our institute explored the use of a reactive hydride composite (RHC) approach to systematically investigate the effect of varying the xLiBH$_4$ content (x = 0.5, 1, 2, 12 mol%) on 6Mg(NH$_2$)$_2$–9LiH to optimize its thermodynamic and kinetic performances. The optimized 6Mg(NH$_2$)$_2$–9LiH–2LiBH$_4$ composition showed significantly improved reaction kinetics compared to other LiBH$_4$ molar ratios. Full hydrogenation of the system (3.45 wt% H$_2$) could be achieved only in 0.5 hours, and complete dehydrogenation was observed in 1 hour at 180 °C and at 1 bar H$_2$ pressure.[43,44] Although the addition of 2 mol% of LiBH$_4$ effectively improved the thermodynamics and kinetics of this composite system, its reaction rate still remains insufficient for practical applications.

Lightweight additives, such as porous carbon materials, are well-known additives for enhancing reaction kinetics by providing a high active surface area and uniform dispersive properties. Bhatnagar *et al.* studied the effects of single-walled carbon nanotubes (SWCNTs) and graphene nanosheets (GNS) on the NaAlH$_4$–MgH$_2$ system. The composite containing 0.5 wt% SWCNTs and 1.5 wt% GNS showed a synergistic effect, enhancing the thermal conductivity and dispersion, which in turn improved both hydrogenation and dehydrogenation kinetics.[45] In addition, various carbon structures, such as graphite, carbon nanofibers, carbon nanotubes and C60, have been used as additives to improve the reaction kinetics of hydrogen storage materials.[46,47]

In this study, mesoporous carbon (CMK-3) was incorporated as an additive in the 6Mg(NH$_2$)$_2$–9LiH–2LiBH$_4$ system to enhance its reaction kinetics. CMK-3 was chosen due to its light weight, high surface area ($\geq$900 m^2 g^{-1}), mesoporous structure (pore diameter: 3.8–4.0 nm) and excellent thermal conductivity.[48] The system was investigated using a combination of experimental techniques, including a Sieverts-type apparatus for measuring hydrogen sorption kinetics, synchrotron radiation X-ray powder diffraction (SR-XRPD) for crystal structure analysis and Fourier transform infrared (FT-IR) spectroscopy for molecular structural analysis. SANS/USANS were utilized to resolve morphological and structural features from the nanometer to micrometer regime, offering critical insights into pore connectivity, particle aggregation and nanoscale restructuring during the dehydrogenation/hydrogenation cycle.[49,50] Quasi-elastic neutron scattering (QENS), on the other hand, probes anion dynamics, providing direct insights into diffusive and reorientational motions on the picosecond to nanosecond timescales.[51,52] These dynamic measurements have proven to be essential for understanding ion transport mechanisms and hydrogen mobility in complex hydrides.[53] To the best of our knowledge, this is the first study that integrates SANS/USANS and QENS analyses to provide a comprehensive understanding of structural evolution and anion dynamics across multiple length and time scales. Together, these complementary techniques allow us to correlate mesoscale morphology, crystallographic evolution and anion dynamics with enhanced hydrogen sorption kinetics in the CMK-3-modified 6Mg(NH$_2$)$_2$–9LiH–2LiBH$_4$ system.

2. Experimental

2.1. Material synthesis

Magnesium amide (Mg(NH$_2$)$_2$, 95% purity) was synthesized in-house *via* a two-step process. Initially, magnesium hydride (MgH$_2$, 95% purity, Rockwood Lithium GmbH) was ball-milled at 400 rpm with a ball-to-powder ratio (BPR) of 40 : 1 in a stainless-steel high-pressure milling vessel (Evico GmbH). The milling was performed under 7 bar ammonia (NH$_3$) gas for 24 hours, with NH$_3$ being refilled every 6 hours to maintain pressure and enhance the reaction kinetics. The intermediate product was subsequently transferred to a high-pressure reactor (Parr Instrument Company) and heat treated at 310 °C under 7 bar NH$_3$ for 48 hours to complete the conversion and maximize the yield of Mg(NH$_2$)$_2$. The purity of the synthesized Mg(NH$_2$)$_2$ was evaluated using the DTA/TGA method. Thermogravimetric analysis performed in the temperature range from room temperature to 600 °C showed a total weight loss of ~39.75 wt%. This value agrees well with the theoretical weight loss (~40 wt%) expected for the decomposition reaction 3Mg(NH$_2$)$_2$ to Mg$_3$N$_2$, indicating an estimated sample purity of ~95%.[54]

For the synthesis of 6Mg(NH$_2$)$_2$–9LiH–2LiBH$_4$-RHC, magnesium amide (Mg(NH$_2$)$_2$), lithium hydride (LiH, 98%, Alfa Aesar) and lithium borohydride (LiBH$_4$, 95%, Sigma-Aldrich) were mixed in a molar ratio of 6 : 9 : 2. The mixture was ball-milled for 36 hours at a BPR of 60 : 1 in a stainless-steel high-pressure milling vessel to ensure homogeneous mixing and mechanical activation. This composite is hereafter referred to as 6 : 9 : 2-RHC.

Structured mesoporous carbon (CMK-3, 99.6% purity, ACS Material) was incorporated into 6 : 9 : 2-RHC at an optimized content of 10 wt%. The resulting mixture was further ball-

milled for 3 hours under similar conditions to achieve a homogeneous dispersion of carbon within the composite. Prior to use, CMK-3 was activated by heating at 120 °C for 12 hours to remove moisture and impurities. This carbon-containing composite is referred to as 6 : 9 : 2-RHC + 0.1CMK3. Pure 6 : 9 : 2-RHC was also further ball-milled for 3 hours to ensure that both materials underwent the same milling treatment.

All sample preparations, handling and storage were performed under an inert atmosphere in an MBRAUN glove box with purified argon (O_2 < 0.1 ppm; H_2O < 0.1 ppm) to avoid sample contamination from air and moisture.

2.2. Thermal analysis

Thermal behavior and gas evolution during the dehydrogenation reactions were analyzed using a Netzsch STA 409 C Differential Thermal Analyzer (DTA) coupled with a Hiden Analytical HAL 201 Mass Spectrometer (MS), situated inside an argon glovebox. Approximately 10 mg of sample was placed in an Al_2O_3 crucible and heated from room temperature (RT) to 300 °C at a heating rate of 5 °C min^{-1}. The experiments were conducted under a continuous flow of argon gas at 50 ml min^{-1}. The DTA instrument was coupled to a Hiden Analytical HAL 201 mass spectrometer (MS) *via* a 1.5 m heated glass capillary. The transfer line was kept at elevated temperature to prevent condensation of evolved gases. Because of the capillary length and the resulting gas transport time, a systematic delay occurs between the thermal events detected by the DTA and the corresponding MS signals. To account for this offset, the MS signal temperature was estimated by correlating the MS detection time with a programmed DTA heating rate (5 °C min^{-1}), enabling an approximate assignment of the gas-evolution temperatures. During dehydrogenation, the evolved gases such as hydrogen (H_2) and ammonia (NH_3) were analyzed by using a mass spectrometer.

Dehydrogenation activation energy (E_a) was determined by running DTA measurements at different heating rates (β) of 1, 2, 5 and 10 °C min^{-1}. The peak temperature (T_m) for maximum heat flow was extracted for each measurement performed at different heating rates. E_a was then calculated using the Kissinger method (eqn (1)), as follows.[55]

$$\ln(\beta/T_m^2) = \ln(AR/E_a) - E_a/RT_m \tag{1}$$

where A is the pre-exponential factor and R (8.314 J K^{-1} mol^{-1}) is the gas constant. The linear relationship between $\ln(\beta/T_m^2)$ and $1/T_m$ was plotted, and the slope ($m = -E_a/R$) of the fitted line was used to determine the value of E_a.

2.3. Hydrogen storage analyses

The isothermal dehydrogenation and hydrogenation kinetics were studied using a custom-built sieverts-type apparatus, capable of operating within a pressure range of 0.01–160 bar and a temperature range of RT–500 °C. For each experiment, approximately 200 mg of sample was loaded into a stainless-steel sample holder inside a glovebox. Dehydrogenation cycles were performed at 180 °C and 1 bar H_2 pressure, while

hydrogenation cycles were conducted at 180 °C and 80 bar H_2. Hydrogenation/dehydrogenation kinetic reaction was also performed at a lower temperature of 140 °C while maintaining the same pressure conditions. Temperature and pressure were controlled with a precision of ±1 °C and ±1 bar, respectively.

2.4. Kinetic modelling

The Sharp and Jones method was applied to determine the rate-limiting step in the dehydrogenation/hydrogenation process of 6 : 9 : 2-RHC and 6 : 9 : 2-RHC + 0.1CMK3. In this approach, experimental data are fitted using eqn (2) as follows.[56]

$$F(\alpha) = A(t/t_{0.5}) \tag{2}$$

Here, α denotes the reaction fraction, defined as the ratio of hydrogen released at a given time to the maximum storage capacity of the material. Parameter 'A' represents the apparent rate constant, and $t_{0.5}$ corresponds to the time at which $\alpha = 0.5$, *i.e.*, 50% of the total reaction has occurred. The analysis primarily focused on the region between 10% and 80% conversion to avoid potential inaccuracies at the initial and final stages of the reaction. By applying different rate equations, several plots of $(t/t_{0.5})_{theoretical}$ *versus* $(t/t_{0.5})_{experimental}$ were obtained. Here, we mainly focused on the Johnson–Mehl–Avrami (JMA) kinetics model, for which equations and their descriptions (F1–F5) are listed in SI Table S1. The Sharp and JMA kinetic models offer a systematic way to decompose the overall reaction kinetics into contributions from different physical processes (interface movement, diffusion in various geometries, nucleation or a combination thereof).[56,57] The best fitting reaction rate model must obey the following rules: the slope of the fitted line should be 1, the *y*-intercept near 0 and a correlation coefficient (R^2) approaching 1.[58]

2.5. Structural analysis

The composition of the samples was analyzed by synchrotron radiation X-ray powder diffraction (SR-XRPD) measurements, which were performed at the side station of P07 beamline operated by the Helmholtz-Zentrum Hereon at PETRA III of Deutsches Elektronen-Synchrotron (DESY), Hamburg, Germany.[59] A monochromatic X-ray beam with a wavelength of 0.14235 Å was employed, and diffraction patterns were collected using a PerkinElmer detector (pixel size of 0.2 mm × 0.2 mm; array of 2048 × 2048 pixels) placed at a sample-to-detector distance of ~1200 mm. The powder samples were prepared in an argon-filled glovebox and subsequently loaded into a circular aluminum sample holder with a diameter of 5 mm and a thickness of 1 mm. The holder was sealed on both sides with Kapton windows to ensure an airtight environment and to preserve sample integrity during measurements. Data acquisition was carried out with a 1 minute exposure per sample scan and 20 seconds of exposure for dark scans. The acquired two-dimensional diffraction data were processed using *FIT2D*,[60] with background subtraction and removal of the Kapton contribution prior to further analysis. The results were compared with reference data from the *ICSD* database.

The crystallite size was estimated using the Scherrer equation (eqn (3)) given below.[61]

$$D = K\lambda/\beta \cos \theta \qquad (3)$$

where D is the crystallite size, K is the shape factor (typically 0.9), λ is the X-ray wavelength (0.014234 nm), β is the full width at half-maximum (FWHM) in radians calculated using diffraction peak fitting and θ is the Bragg angle. The complete calculation is provided in SI Table S2.

An Agilent Technologies Cary 630 FT-IR spectrometer was used within an argon-filled glovebox to characterize the N–H and B–H stretching vibrations. Infrared spectra were collected in transmission mode over the spectral range of 2000–3500 cm^{-1} with a resolution of 4 cm^{-1}.

Small-angle and ultra-small-angle neutron scattering (SANS/USANS) experiments were conducted at the Australian Nuclear Science and Technology Organization (ANSTO) facility at Lucas Heights using the Quokka SANS instrument and Kookaburra USANS instrument, respectively.[62,63] Sample preparation was performed in the ANSTO chemistry laboratory in a helium-filled glovebox which was controlled with continuous helium flow to avoid any risk of contamination and to ensure experimental reproducibility. A monolayer of powder was applied to Kapton tape using a brush and subsequently secured with a second layer of Kapton tape to ensure positional stability during the measurement process. The encapsulated samples were then mounted into demountable aluminum cells between two parallel quartz glass windows (19 mm in diameter, with high transmission and low level of scattering).[64] The sample holders were subsequently transferred to the SANS/USANS beamline and positioned on a motorized rail system, ensuring precise alignment and enabling the neutron beam to pass through the sample volume during measurements. The Kookaburra instrument was equipped with a highly oriented pyrolytic graphite (HOPG) crystal, as a pre-monochromator, which delivers two different wavelengths λ to the instrument: $\lambda_{Si}(111) = 4.74$ Å and $\lambda_{Si}(311) = 2.37$ Å. Our USANS measurements were conducted using a 29 mm aperture and neutron wavelength of 4.74 Å, covering a q range of 4×10^{-5} to 8×10^{-4} Å^{-1} to have an adequate overlap with the SANS data. The Quokka instrument was equipped with a high count rate, 1 m^2 position-sensitive detector (pixel size: 5 mm), developed by Brookhaven National Laboratory. It employs a neutron velocity selector to produce a continuously tunable range of incident neutron wavelengths spanning from 4.5 Å to 40 Å, with a corresponding wavelength resolution ranging between 7% and 18%, depending on the neutron velocity selector tilt angle. Prior to data acquisition, the detector efficiency was calibrated using a polymethyl methacrylate (PMMA) standard. SANS measurements were performed at three distinct sample-to-detector distances (SDD = 1.3 m, 12 m, and 20 m with MgF$_2$ lenses). The incident neutron wavelength was set to 5 Å for measurements at 1.3 m and 12 m SDD. For measurements at 20 m SDD, the wavelength was set to 8.1 Å to optimize coverage of the q-range of interest. Additionally, measurements of the direct (empty) beam, the blocked beam, and an empty sample holder were conducted to enable accurate background subtraction and transmission corrections. For absolute intensity calibration, a water standard of known scattering cross-section was measured as well.

The SANS data acquired at three different SDDs were processed and merged using the standard Quokka data reduction macros implemented within the *Igor Pro* software environment.[65] USANS data were then desmeared and subsequently merged with the reduced SANS data.[66,67] Lastly, data analysis and model fitting were performed using the *SASfit* and *SASView* software packages.[68,69] Six different samples were studied; 6 : 9 : 2-RHC and 6 : 9 : 2-RHC + 0.1CMK3, each in ball-milled, thermally desorbed and absorption states, to explore structural evolution under different hydrogen sorption conditions.

2.6. Dynamic analysis

QuasiElastic Neutron Scattering (QENS) is a neutron spectroscopy technique used to study low-energy motions, such as relaxations and diffusions, with energy transfers typically less than 1 meV. These types of motions show a quasielastic profile centered on elastic scattering, *i.e.* zero energy transfer, with small energy changes. The quasielastic signal appears as broadening around the elastic line and arises from stochastic, non-periodic motions of atoms per molecules.[70] It provides valuable insights into the molecular dynamics of hydrogen-containing units occurring on the picosecond timescale and angstrom length scale.[71] QENS experiments were conducted on 6 : 9 : 2-RHC and 6 : 9 : 2-RHC + 0.1CMK3 samples in the desorbed state using the IN5 time-of-flight cold neutron spectrometer at the Institute Laue-Langevin (ILL), Grenoble, France.[72,73] Approximately 400 mg of each sample was loaded into hollow cylindrical sample holders, with a 0.5 mm gap between the inner and outer cylinders. The outer cylinder had a diameter of 15 mm, ensuring optimal sample thickness and uniform neutron transmission during the experiment. Measurements were performed at −73 °C, 25 °C, 100 °C, and 200 °C temperatures using a cryofurnace, with incident neutron wavelengths of 4.9 Å and 8 Å, covering a momentum transfer range of 0.2–2.5 Å^{-1}. Vanadium standards and empty sample holders were used for resolution and background correction. Data reduction was conducted using *MANTID*, while data analysis was performed using *DAVE* software.[74,75]

The measurements were performed at two energy resolutions, 80 μeV and 20 μeV (full width at half-maxima), corresponding to observable timescales ($t_{obs} = 2\hbar/\text{FWHM}$) of ~16 ps and ~66 ps, respectively. The experiments probed molecular motions of hydrogen-containing groups ([BH$_4$]$^-$ and [NH$_2$]$^-$) within the 6 : 9 : 2-RHC and 6 : 9 : 2-RHC + 0.1CMK3 systems over a temperature range of −73 °C to 200 °C, aiming to understand the effect of CMK-3 on the system's absorption and desorption properties. The measured signal, dominated by hydrogen's incoherent scattering cross-section, reflects the dynamic structure factor $S(Q, \omega)$, which probes the self-correlation function of hydrogen atoms, capturing both long-range motions (*e.g.*, diffusion) and localized dynamics (*e.g.*, molecular rotations). If the probed atoms remain immobile, the scattering function $S(Q, \omega)$ consists solely of an elastic peak centered at

zero energy transfer, which can be represented by a delta (δ) function. In contrast, when atomic or molecular dynamics are present, then the quasielastic components appear and are typically modeled with one or more Lorentzian functions.[70]

3.   Results

Thermal behavior of 6 : 9 : 2-RHC and 6 : 9 : 2-RHC + 0.1CMK3 was studied using differential thermal analysis (DTA). The DTA measurements were conducted at a heating rate of 5 °C min^{-1} from RT up to 300 °C (Fig. 1a). The DTA thermogram of the pure sample shows two distinct endothermic peaks. The minor peak (peak 1, zoom in) observed at ~115 °C corresponds to the polymorphic phase transition of $LiBH_4$ from its orthorhombic to hexagonal crystal structure.[76]

The subsequent thermal event (peak 2) is the main dehydrogenation process. In contrast, the sample containing CMK-3 exhibited a single dehydrogenation peak at approximately 170 °C, 10 °C lower than the pure system. The characteristic endothermic event of the $LiBH_4$ polymorphic phase transition was not detected. This observation may indicate the interaction of $LiBH_4$ with other components, consistent with previous results. The reaction could occur with $LiNH_2$ formed from the reaction of $Mg(NH_2)_2$–LiH and leads to the formation of a solid solution based on $LiBH_4$ and $LiNH_2$.[38] The gases released during thermal events were analyzed using a mass spectrometer (MS) (Fig. 1b). In both samples, H_2 is identified as the primary evolved gas. However, in the case of 6 : 9 : 2-RHC, a minor NH_3 release is observed at temperatures above 220 °C, whereas the 6 : 9 : 2-RHC + 0.1CMK3 composite suppressed the NH_3 signal over the entire investigated temperature range.

To investigate the underlying origin of the improved reaction kinetics in the CMK-3 modified system, the apparent activation energies (E_a) of both the pristine and modified composites were determined using Kissinger's method.[55] The peak reaction temperatures (T_m), determined from DTA measurements at different heating rates (1, 2, 5 and 10 °C min^{-1}), were used in eqn (3). The corresponding DTA curves are provided in SI-

Fig. S1. The linear relationship between $\ln(\beta/T_m^2)$ and $1/T_m$ was plotted, and the slope of the fitted line was used to determine the value of E_a (Fig. 2). The activation energy for the dehydrogenation process of the pure system was found to be 117 ± 1 kJ mol^{-1}, while the sample modified with CMK-3 showed a reduced activation energy of 106 ± 2 kJ mol^{-1}. Therefore, the improved reaction kinetics observed in the composite system upon incorporation of CMK-3 can be attributed to a reduction in the apparent activation energy, which suggests a lowering of the energy barrier associated with the rate-limiting step.

To further validate the implied reduction in the energy barrier associated with the rate-limiting steps, isothermal volumetric measurements were conducted to monitor the dehydrogenation/hydrogenation reaction kinetics of both composite systems. The isothermal dehydrogenation and hydrogenation performance of the pure system and the samples incorporated with CMK-3 were measured at 180 °C. As can be seen in Fig. 3a, the kinetics of hydrogen uptake and release of
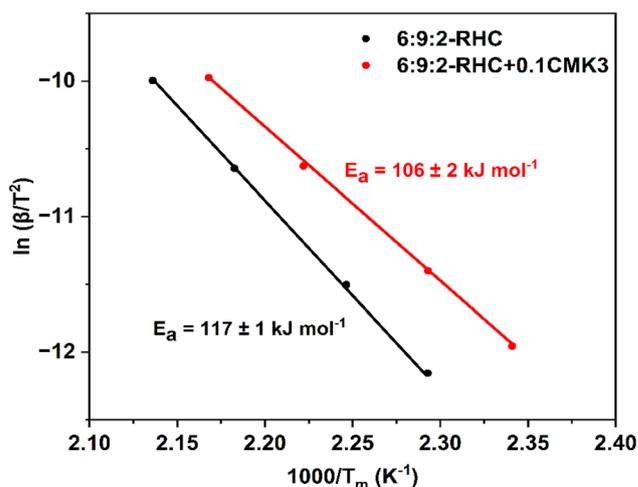

Fig. 2 Calculation of activation energy derived from DTA with different heating rates (1, 2, 5 and 10 °C min^{-1}) using the Kissinger method.
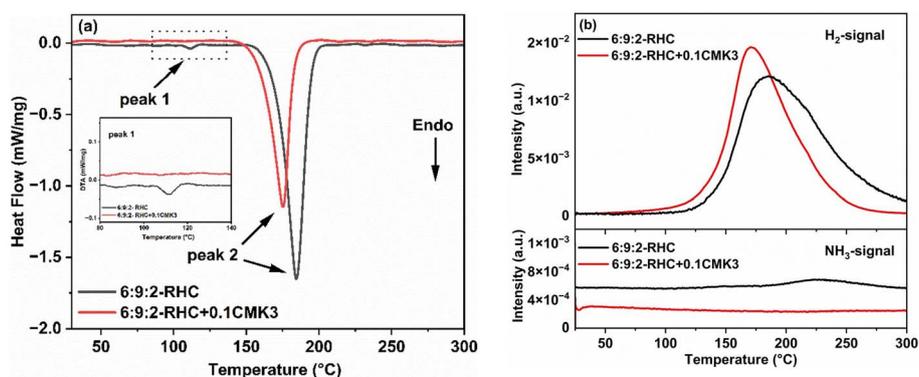

Fig. 1 DTA curves of 6 : 9 : 2-RHC and 6 : 9 : 2-RHC + 0.1 CMK3 in the temperature range of 25−300 °C with a heating rate of 5 °C min^{-1} (a). MS graphs showing the evolution of hydrogen and ammonia gases during thermal events (b).
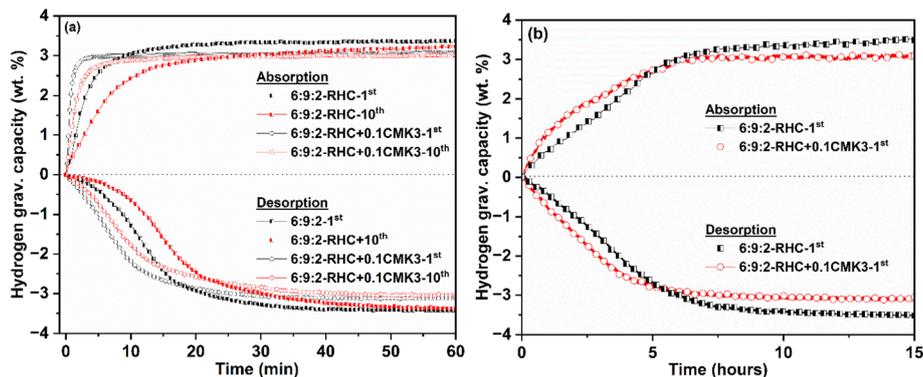
Fig. 3 First and tenth isothermal dehydrogenation at 180 °C and 1 bar and hydrogenation at 180 °C and 80 bar of 6 : 9 : 2-RHC and 6 : 9 : 2-RHC + 0.1CMK3 (a). First dehydrogenation and hydrogenation at 140 °C, under the same pressure conditions (b).

6 : 9 : 2-RHC + 0.1CMK3 are significantly improved, reconfirming and solidifying the above results obtained by calorimetry. The absorption kinetics show a remarkable acceleration as compared to the pristine material. During the first hydrogenation cycle, 3 wt% of hydrogen is absorbed in only 3 minutes, while the pure sample requires over 30 minutes to reach the full capacity. The dehydrogenation of the modified material reaches 3 wt% of hydrogen within 25 minutes, whereas the pure system takes approximately 60 minutes. Moreover, the hydrogenation and dehydrogenation kinetics of the CMK-3 modified system remain almost unchanged after ten cycles, whereas the kinetics of the pure system decreases significantly.

As shown in Fig. 3b, hydrogenation and dehydrogenation can also be achieved at lower temperatures of 140 °C, with a faster rate as compared to the pure material. This improvement highlights the catalytic role of CMK-3, which promotes more efficient hydrogen transfer and enhances the overall reaction kinetics even at lower temperatures.

To assess the improved reversibility and cycling stability of the CMK-3-modified system, ten consecutive isothermal volumetric desorption–absorption cycles were performed on both the pure and CMK-3 modified materials (SI-Fig. S2 and S3). 6 : 9 : 2-RHC + 0.1CMK3 exhibited a reversible hydrogen storage capacity of ~3 wt% with 98% capacity retention over the first ten cycles with much faster kinetic rates (SI-Fig. S4), whereas the pure system retained only 90% of its initial capacity under the same conditions. These results clearly demonstrate that CMK-3 significantly helps in enhancing both the reversibility and long-term cycling performance of the material.

To elucidate the evolution of the rate-limiting steps during the hydrogenation and dehydrogenation processes of 6 : 9 : 2-RHC and 6 : 9 : 2-RHC + 0.1CMK3, the Johnson–Mehl–Avrami (JMA) kinetic model was applied to both the first and ninth reaction cycles. The application of this model, which describes transformation kinetics governed by nucleation and subsequent growth mechanisms, aimed to assess potential changes in the reaction pathway over multiple dehydrogenation/hydrogenation cycles. Specifically, various forms of the JMA model (F1–F5; see SI-Table S1 for more details) were evaluated to determine the best fit to the experimental data and to identify the underlying kinetic mechanism. For 6 : 9 : 2-RHC, the dehydrogenation reaction during both the first and ninth cycles followed the F2 JMA model, whereas the hydrogenation cycles were best described by the F1 model (SI-Fig. S5–S8).

These findings align well with a previous study reported by Gizer et al.[43] The F1 model indicates a mechanism involving random nucleation and one-dimensional interface-controlled growth, where the reaction rate is limited by the movement of the phase boundary (Table 1). In contrast, the F2 model represents a random nucleation mechanism coupled with two-dimensional diffusion-controlled growth, where diffusion of species dictates the reaction rate. Similarly, for 6 : 9 : 2-RHC + 0.1CMK3, the reactions follow the same kinetic models as 6 : 9 : 2-RHC, as shown in SI-Fig. S9–S12.

Investigating the reaction pathways on the atomistic scale during the dehydrogenation/hydrogenation process, SR-XRPD and FTIR analyses were carried out. The combined use of both analysis techniques enabled the identification of both

Table 1 Rate limiting process derived by using the Sharp and Jones method[a]

Sample	Dehydrogenation		Hydrogenation	
	1st	9th	1st	9th
6 : 9 : 2-RHC	F2	F2	F1	F1
6 : 9 : 2-RHC + 10CMK3	F2	F2	F1	F1

[a] F1: JMA, $n = 1$, interface controlled – 1D growth with an interface-controlled reaction rate. F2: JMA, $n = 2$, diffusion controlled – 2D growth of existent nuclei at a constant interface rate.
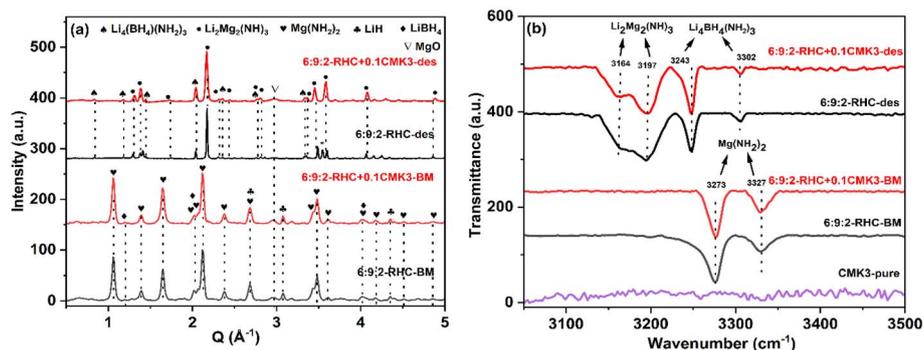
Fig. 4 XRD patterns of 6 : 9 : 2-RHC and 6 : 9 : 2-RHC + 0.1CMK3 as milled and after first desorption (a). FTIR spectra of 6 : 9 : 2-RHC and 6 : 9 : 2-RHC + 0.1CMK3 as milled and after first desorption (b).

crystalline and amorphous phases present in the samples. SR-XRPD patterns of the ball-milled 6 : 9 : 2-RHC and 6 : 9 : 2-RHC + 0.1CMK3 confirmed the presence of the reactants $Mg(NH_2)_2$, LiH and $LiBH_4$ with no detectable crystalline carbon-containing phases (Fig. 4a). After the first dehydrogenation step, both samples show diffraction peaks corresponding to dehydrogenated products, $Li_4(BH_4)(NH_2)_3$ and $Li_2Mg_2(NH)_3$, consistent with the literature.[9,32] In agreement with the as-milled sample, no evidence of interaction between the carbon additive and the reaction products was detected. This indicates that the ball milling process effectively facilitates only the homogeneous dispersion of the carbon additive throughout the material but does not affect its chemical state.[77] SR-XRPD analysis of samples in the ball-milled state and after first hydrogenation state confirms the presence of reactants, again with full reversibility of the dehydrogenation/hydrogenation cycle (SI-Fig. S13a). We detected a minor peak belonging to Mg–O because of sample surface oxidation during the measurements. The average crystallite sizes of 6 : 9 : 2-RHC and 6 : 9 : 2-RHC + 0.1CMK3 were calculated from the SR-XRPD data using the Scherrer equation (eqn (3)). In the ball-milled state, the pristine composite exhibited an average grain size of approximately 14 nm, while the CMK-3 modified sample showed a slightly smaller size of ~13.3 nm, indicating effective refinement during mechanical milling (SI-Table S2). After the first dehydrogenation cycle, the crystallite size of the pristine sample increased to ~25 nm, whereas the CMK-3 containing composite retained a finer grain size of ~19 nm, suggesting that CMK-3 effectively suppresses grain coarsening during hydrogen release.

FT-IR analysis was carried out to reconfirm the presence of reactants and products as observed by XRPD. FT-IR spectra were recorded in the range of 3000–3500 cm^{-1} for clarity in eluci-dating the reaction mechanism (Fig. 4b). The FT-IR spectra of pure and CMK-3 modified materials in the as-milled state confirm the N–H stretching vibrations of $Mg(NH_2)_2$ at 3273 and 3327 cm^{-1}. In the desorbed state, the samples show a broad band with two distinct peak positions at 3164 and 3197 cm^{-1}, which belongs to $Li_2Mg_2(NH)_3$. Additionally, characteristic peaks at 3243 and 3302 cm^{-1} confirm the presence of $Li_4(BH_4)(NH_2)_3$, consistent with the literature reports.[9] The BH_4^- stretching vibrations of $LiBH_4$ in the ball-milled state and of the

BH_4^- units in $Li_4(BH_4)(NH_2)_3$ after desorption were also iden-tified (SI-Fig. S13b). SR-XRPD and FT-IR results suggest that the hydrogen storage in this system proceeds through a specific reaction mechanism, as explained below (eqn (4)), without any interaction with the additive CMK-3.

$$6Mg(NH_2)_2 + 9LiH + 2LiBH_4 \leftrightarrow 3Li_2Mg_2(NH)_3$$
$$+ Li_4(BH_4)(NH_2)_3 + LiBH_4 + 3H_2 \quad (4)$$
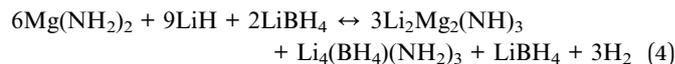
X-ray diffraction (XRD) provides information on the crystal structure and phase composition; on the other hand, Fourier transform infrared (FT-IR) spectroscopy probes functional groups and local bonding environments at the atomic and molecular scales. To gain more detailed understanding about how CMK-3 influences the nano- and microstructures of the composite system, we carried out SANS/USANS analysis. Combined SANS/USANS cover a broad Q-range (from ~10^{-4} to ~1 Å^{-1}), which allows the probing of structural features from micrometers down to a few nanometers.

The following section presents the SANS/USANS results in a chronological and comparative framework, beginning with the as-milled samples, followed by those subjected to an initial desorption and concluding with samples that have undergone a full dehydrogenation–hydrogenation cycle. The scattering profiles were analyzed across the full accessible Q-range, which allow the characterization of structural features from the mesoscale to the nanoscale. To systematically highlight and compare the structural features, the scattering curves are segmented into defined Q-intervals in the following analysis. Fig. 5 displays the SANS/USANS scattering curves for the pure and CMK-3 incorporated samples in the ball-milled state, alongside the curve for the pristine CMK-3 material, which serves as a structural reference. For clarity, the scattering curve of the CMK-3 reference was downscaled by a factor of 1.5 for comparison. Upon initial inspection of all scattering profiles, one can observe that the scattering curves of both composites exhibit different scattering regions with distinct scattering behaviors.

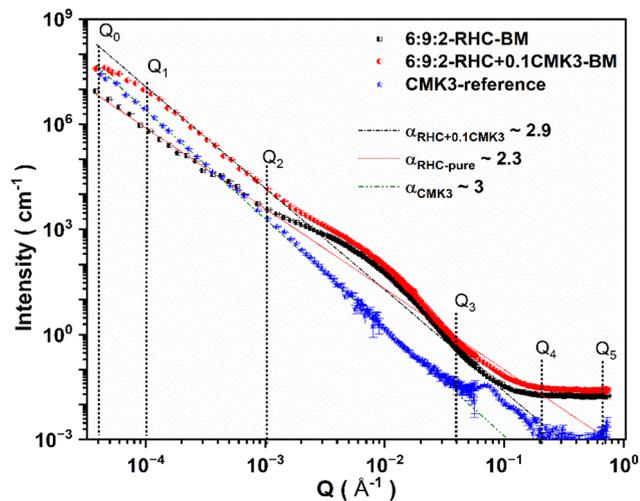$$I(Q) = I_l + I_m + I_h + B \quad (5)$$

Fig. 5 SANS/USANS scattering profiles of the pristine 6 : 9 : 2-RHC and CMK-3 modified 6 : 9 : 2-RHC + 0.1CMK3 composites in the ball-milled state, along with the as-received CMK-3 reference sample.

where I_l describes the intensity behavior in the low Q-region, spanning between the USANS and the low Q-limit of the SANS regime. I_m and I_h represent the scattering intensities of the intermediate and high Q ranges, respectively. Additionally, incoherent neutron scattering from hydrogen atoms in the samples contributes to a constant isotropic background B, which can be observed as a uniform intensity offset. In the USANS to the beginning of the SANS region, the scattering intensity behavior of both samples reflects the differences in mesoscale structural features in this regime, such as aggregate compactness or hierarchical organization. Indeed, a comparison of the scattering profiles for all three samples in this region reveals a consistent power-law decay, extending over nearly one order of magnitude in Q ($\sim 10^{-4}$ to 10^{-3} Å^{-1}), indicating the presence of fractal-like structural correlations over a decade of length scale. Therefore, the scattering intensity in this region can be expressed as:

$$I_l(Q) \propto Q^{-\alpha} \qquad (6)$$

Notably, the CMK-3 incorporated sample shows a slight deviation from this ideal power-law behavior ([Q_1; Q_2]), which occurs only at Q_1 within the interval [Q_0; Q_1] < 10^{-4} Å^{-1}, suggesting modifications in long-range structural order. In contrast, the pure sample after milling follows an ideal power-law behavior over a large range of Q [Q_0; Q_1] with an exponent of $\alpha \approx 2.3$ (dotted red line). This decay exponent is characteristic of an open mass fractal structure composed of loosely connected aggregates with a relatively low spatial connectivity. In contrast, the 6 : 9 : 2-RHC + 0.1CMK3 sample exhibits a relatively higher scattering decay exponent ($\alpha \approx 2.9$; dash-dot black line) across the probed Q-range, indicating a transition toward a more densely connected mass fractal network.[78,79] For reference, the scattering profile of the pure CMK-3 sample has

a scattering decay exponent of $\alpha \approx 3.0$ (dash-dot green line), consistent with a morphology intermediate between a highly compact mass fractal and a rough surface fractal. Notably, the 6 : 9 : 2-RHC + 0.1CMK-3 composite matrix exhibits a significantly higher scattering decay exponent compared to the pure composite; it is very close to the exponent value of the pure CMK-3 reference sample. This elevated decay exponent in the 6 : 9 : 2-RHC + 0.1CMK3 sample reflects a more compact, self-similar aggregate morphology characterized by increased spatial density and enhanced structural connectivity over extended length scales. The similarity in the scattering exponent between the CMK-3 modified composite and the pristine CMK-3 reference suggests that the carbon additive retains its intrinsic hierarchical, fractal-like architecture, despite undergoing mechanical incorporation into the hydride components through high-energy ball milling. More importantly, the presence of CMK-3 appears to significantly influence the structural organization of the composite, acting as a framework that constrains or directs the spatial distribution of the hydride phase. This templating effect governs the development of hierarchical features over a broad range of length scales, from a few microns down to several hundred nanometers.

In the intermediate Q-range, both the pure and modified composites exhibit a broad Bragg-like shoulder after the milling process, extending across a broad Q region (roughly within the interval [Q_2; Q_3]), indicative of structural order typically associated with phase domains of some shape and sizes. The scattering behavior in this region, therefore, can be expressed as:

$$I(Q)_m \propto (\Delta\rho_m)^2 \times V_m^2 \times P_m(Q) \times S_m(Q) \qquad (7)$$

In this context, $\Delta\rho_m$ denotes the difference in the scattering length density (SLD) between two phases. This difference is defined as the scattering "contrast". The volume of the scattering object is denoted as V_m, while $P_m(Q)$, the so-called form factor, characterizes the internal shape and size of individual scatterers. Interparticle interactions are described by the structure factor, $S_m(Q)$. The unaltered position and profile of the shoulder, however, indicate that the incorporation of CMK-3 does not substantially modify the spatial correlations at these length scales. The characteristic size of the associated structural features was estimated, by fitting the region with the shape-independent Guinier–Porod model (eqn (8)).[80]

$$I(q) = \begin{cases} \dfrac{G}{Q^s} \exp\left[\dfrac{-Q^2 R_g^2}{3-s}\right] & Q \le Q_1 \\[2mm] D/Q^m & Q \ge Q_1 \end{cases} \qquad (8)$$

This is based on the generalized Guinier law,[81] and by using this equation and optimizing the parameter $\delta = 3 - s$, we can estimate the shape of the objects. If $\delta = 3$, then the Guinier–Porod equation (eqn (8)) transforms the standard Guinier formula for spherical objects. Similarly, when $\delta = 2$, the shape of the objects can be approximated by rod-like structures, and lastly if $\delta = 1$ the objects can be assumed as lamellae or platelets, respectively. The quantities Q_1 and D in eqn (8) are

determined using the continuity conditions of the Guinier and Porod functions and their derivatives:

$$Q_1 = \frac{1}{R_g}\sqrt{(m-s)(3-s)/2} \tag{8.1}$$

$$D = \frac{G}{R_g^{m-s}}\exp\left[-\frac{m-s}{2}\right]\left(\frac{(m-s)(3-s)}{2}\right)^{\frac{m-s}{2}} \tag{8.2}$$

The model was fitted on $6:9:2$-RHC and $6:9:2$-RHC + 0.1CMK3 scattering curves (SI-Fig. S14a and b), respectively. The fit parameters for the pure system resulted in $R_g \approx 8.2$ nm and $s \approx 1.7$, and similarly the parameters of the model fitting of $6:9:2$-RHC + 0.1CMK3 resulted in $R_g \approx 8$ nm and $s \approx 1.8$. The dimensionality parameter δ of the pure system is roughly 1.3, and the one for the CMK-3 modified system is 1.2. These values of δ suggest that the shape of the structures is in both samples more like plates. The dimension of the structures in this region can be estimated, as a first approximation, to $D \sim 60$ nm, using the following formula:

$$D \approx 2\pi/Q \tag{9}$$

While the shape and position of the scattering feature in this intermediate Q range remain nearly identical in both samples, the scattering profile of the modified sample shows consistently higher scattering intensity over the entire Q-range. Considering the overall similarity of the scattering profiles of both samples across most of the Q-range, with notable deviations only at very low and very high Q values, the increased scattering intensity observed in the CMK-3 incorporated sample can be attributed to the presence of CMK-3 additive at these length scales, which introduces additional scattering contrast due to its distinct scattering length density in eqn (7). To estimate the contrast for both hydride composites in this Q region, a simple multiphase physical mixture model can be assumed as a first-order approximation:

$$I(Q)_m \propto (\Delta\rho_m)^2 = \sum_{i=1}^{N}\sum_{j=1}^{N}\phi_i\phi_j(\rho_i - \rho_j)^2 \tag{10}$$

Here, ϕ_i denotes the volume fraction of the ith phase and ρ_i its corresponding scattering length density (SLD). Using eqn (7), the relative scattering intensities of the pure and CMK-3 modified samples can be estimated. Based on the calculated average contrast values, the modified composite exhibits a scattering intensity that is approximately 1.5 times greater than that of the pure composite, which is in good agreement with the experimentally obtained results shown in Fig. 5.

Examination of the high Q region (Porod regime; $[Q_3; Q_4]$) in the scattering profiles of the as-milled samples reveals minor variations in intensity. To enhance the visibility of subtle differences and facilitate a more qualitative comparison, the corresponding curves were re-plotted in a Kratky representation (Fig. 6), together with the CMK-3 reference profile for context.

For the sake of visual clarity in comparison, the scattering curve of the CMK-3 modified composite in Fig. 6 was
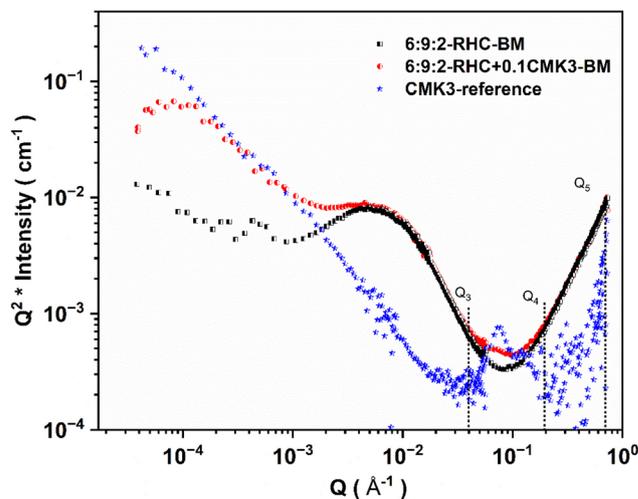

Fig. 6 Kratky plot of SANS/USANS scattering profiles of the pristine $6:9:2$-RHC and $6:9:2$-RHC + 0.1CMK3 composites in the ball-milled state, along with the CMK-3 reference sample.

downscaled by a factor of 1.5. It is worth noting that the Kratky representation shown in Fig. 6 distinctly emphasizes the similarity in fractal scattering characteristics between the as-milled modified composite and the CMK-3 reference, alongside the comparable Bragg shoulder features observed in both the as-milled pure and modified composite samples. Moreover, by examining the scattering curves of both samples in the interval $[Q_3; Q_4]$, a clear deviation in scattering behavior between the pure and modified composites can be observed. The modified sample exhibits a well-defined shoulder with a weakly pronounced maximum, whereas the pure composite displays a decrease in intensity, reaching a local minimum within the same region. Notably, the position of the shoulder maximum of the CMK-3 incorporated sample coincides with the primary Bragg peak of CMK-3, located at $Q \approx 0.07$ Å^{-1}. Applying eqn (9), this peak corresponds to a real-space periodicity of approximately 9 nm. This dimension is associated with the center-to-center spacing of the mesopores in CMK-3, corresponding to the (100) reflection of its two-dimensional hexagonally ordered mesostructure.[82] These findings provide strong evidence that the structural integrity of the CMK-3 additive is maintained at both the micro- and nanoscales, despite the mechanical effects of the ball milling process. The scattering intensities of both samples gradually transition into a flat background in the interval $[Q_4; Q_5]$ at very higher Q-values, effectively masking structural correlations in this regime. Therefore, the scattering intensity can be described in this region by:

$$I(Q)_h + B \propto (\Delta\rho_h)^2 \times V_h^2 \times P_h(Q) \times S_h(Q) + B \tag{11}$$

Here, the structure factor $S_h(Q)$ cannot be neglected due to the embedded and well-maintained structure of CMK-3 in the hydride matrix. Fig. 7a presents the SANS/USANS results of the samples following hydrogen release, with the scattering profile of CMK-3 included for reference. For clarity, the scattering curves of the $6:9:2$-RHC and $6:9:2$-RHC + 0.1CMK3 desorbed
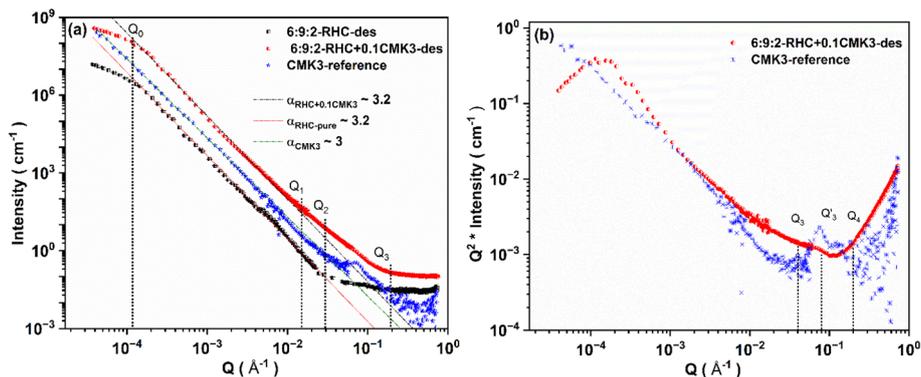
Fig. 7 SANS/USANS scattering profiles of the desorbed 6 : 9 : 2-RHC and desorbed 6 : 9:2-RHC + 0.1CMK3 composites, along with the CMK-3 reference sample (a). Kratky plots of 6 : 9 : 2-RHC + 0.1CMK3 and CMK-3 reference (b).

samples and the CMK-3 reference have been vertically offset by a factor of 1.5. Following the desorption process, both samples display nearly identical scattering profiles across the USANS regime and into an extended portion of the SANS region, beyond which distinct deviations become apparent. Across the entire accessible Q-range, both samples exhibit characteristic power-law scattering behavior, extending from the lowest Q values in the USANS regime to high-Q values in the SANS region. Notably, at roughly $Q_0 \approx 1.12 \times 10^{-4}$ Å^{-1}, a crossover in the power-law behavior can be observed, marking a transition between two distinct power-law regimes. This change in slope indicates a variation in the underlying structural features at different length scales. The characteristic length scale at the crossover point can be estimated to $l \approx 5$ μm, using eqn (13). Below the crossover point Q_0 in the USANS regime ($3.9 \times 10^{-5} \leq Q \leq 1.12 \times 10^{-4}$ Å^{-1}), the scattering intensity follows a shallow power-law decay with an exponent of $\alpha \approx 1.2$, indicative of large-scale, mass-fractal features. This suggests the presence of extended, self-similar, loosely connected structural networks with hierarchical porosity in both samples, which most likely reflect the large-scale agglomeration of the composite domains with domain sizes greater than 5 μm. However, it should be noted that the observed Power-law behavior does not extend over a full order of magnitude within this Q-range, thereby constraining the reliability and accuracy of the structural interpretation and conclusions drawn from this regime.

Above the crossover point, within the $[Q_0; Q_1]$ interval spanning the Q-range between the lower USANS and the intermediate SANS regime ($1.12 \times 10^{-4} \leq Q \leq 1.5 \times 10^{-2}$ Å^{-1}), both samples exhibit a steeper power-law decay in scattering intensity, characterized by an exponent of $\alpha \approx 3.2$. This behavior is indicative of surface-fractal morphology, suggesting that the dominant structural features in this length scale regime (approximately from 40 nm up to 5 μm) are governed by rough/irregular interfaces rather than smooth particle/grain boundaries. In contrast to the desorbed CMK-3 modified sample, the desorbed pure sample maintains the same power-law trend up to $Q_2 \approx 3 \times 10^{-2}$ Å^{-1}, beyond which the scattering intensity levels off to a constant background scattering, indicating the absence of detectable structural features at smaller length

scales. Within the interval $[Q_1 \approx 1.5 \times 10^{-2}$ Å$^{-1}; Q_3 \approx 1.5 \times 10^{-1}$ Å$^{-1}]$ (Fig. 7a), the desorbed sample containing the CMK-3 additive exhibits a pronounced deviation from power-law behavior, characterized by the emergence of a broad Bragg shoulder. Within the interval $[Q_4; Q_5]$, the scattering intensities of both samples gradually transition into flat background scattering. Therefore, the general form of the scattering curve of the desorbed samples can be described as:

$$I(Q) \propto \sum_{i=1}^{2} I_{li}(Q) + \Delta\rho_h^2 \times V_h^2 \times P_h(Q) \times S_h(Q) + B \quad (12)$$

where $I_{li}(Q)$ describes the power-law scattering of the ith segment at low angles. To more clearly highlight the deviation in scattering behavior of the CMK-3 modified composite within the $[Q_1; Q_3]$ range, its scattering curve was replotted in a Kratky representation and compared with that of the CMK-3 reference material (Fig. 7b). This representation emphasizes subtle features associated with structural differences introduced by the additive. As shown in Fig. 7b, the modified sample exhibits a distinct Bragg shoulder within the $[Q_1; Q_3]$ interval, with its peak position coinciding with that of the CMK-3 reference. This alignment provides strong evidence that the characteristic mesoporous ordering of CMK-3 is retained over the desorption process and preserves its structural framework at the nano-metric scale. Furthermore, these results suggest that the presence of CMK-3 additive exerts a significant influence on the nanostructure of the hydride. The results indicate that, during the desorption process, hydride particles/grains with dimensions ranging approximately from 4 to 40 nm are formed and effectively stabilized by the presence of the CMK-3 additive. These nanoparticles are homogeneously distributed among larger, fractured particles, which are assembled into loosely connected networks exhibiting pronounced hierarchical porosity.

In contrast, the pure sample shows no distinct size distribution across either the nanometric or micrometric scales. Instead, it exhibits scale-invariant fractal scattering over the entire Q-range, indicative of surface roughness spanning multiple length scales. A crossover in the USANS regime marks a transition from surface fractal to mass fractal scattering,
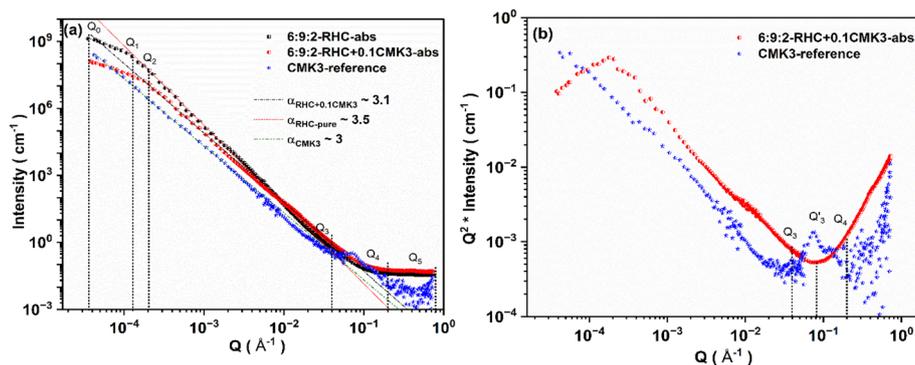
Paper

Fig. 8 SANS/USANS scattering profiles of 6 : 9 : 2-RHC and 6 : 9 : 2 RHC + 0.1CMK3 composites in the absorbed state, along with the CMK-3 reference sample (a). Kratky plots of 6 : 9 : 2-RHC + 0.1CMK3 in the absorbed state and CMK-3 reference (b).

suggesting agglomeration of these particles with rough surfaces to larger, loosely connected mass fractals. To monitor the structural evolution of the pure and modified samples over a complete dehydrogenation–hydrogenation cycle, the desorbed samples were rehydrogenated and were measured by SANS/USANS. The scattering profiles of both samples following one full cycle are presented in Fig. 8a, alongside that of the CMK-3 reference.

For clarity, the scattering curves of CMK-3 reference sample have been vertically shifted. After a full cycle, the scattering profiles of both samples display a fractal-like behavior across the entire accessible Q-range, except at very high Q values where the incoherent scattering dominates the scattering profile. In the hydrogenated (absorbed) state, similar to the desorbed state, both the pure and modified samples exhibit two distinct power-law scattering regimes, indicative of a hierarchical structural organization extending across multiple length scales. The first regime, observed at lower scattering vectors, is characterized by decay exponents in the range $1 < \alpha < 3$, corresponding to mass fractal behavior, where the exponent $\alpha = D_m$ defines the mass fractal dimension D_m. This regime reflects the spatial arrangement and connectivity of self-similar particle agglomerates. In this context, the pristine sample exhibits a power-law decay with an exponent of $\alpha \approx 1.5$ over the interval $[Q_0 \approx 3 \times 10^{-5}; Q_1 \approx 1.3 \times 10^{-4} \text{ Å}^{-1}]$, consistent with moderately compact fractal aggregates of relatively high mass density. In comparison, the CMK-3 modified composite shows a lower exponent of $\alpha \approx 1.2$ across an extended range $[Q_0 \approx 3 \times 10^{-5}; Q_2 \approx 2.1 \times 10^{-4} \text{ Å}^{-1}]$, indicating the formation of looser, more open and weakly connected fractal networks. Furthermore, the crossover to the next scattering regime occurs at a higher scattering vector for the doped sample ($Q_2 \approx 2.1 \times 10^{-4} \text{ Å}^{-1}$, ~3 μm) compared to the pure one ($Q_1 \approx 1.3 \times 10^{-4} \text{ Å}^{-1}$, ~5 μm), implying that the structural correlation length is smaller in the modified system. In the second regime, at higher scattering vectors beyond the respective crossover points, both systems exhibit decay exponents in the range $3 < \alpha < 4$, corresponding to surface fractal behavior, where the surface fractal dimension is defined by $D_s = 6 - \alpha$. This regime probes the morphological complexity and roughness of the particle surfaces. Here, the pure sample demonstrates a steeper decay with $\alpha \approx 3.5$ over the

range $[Q_0; Q_3 \approx 3 \times 10^{-2} \text{ Å}^{-1}]$, yielding a surface fractal dimension of $D_s \approx 2.5$, indicative of moderately rough surface morphologies. In contrast, the modified sample exhibits a gentler decay with $\alpha \approx 3.1$ over the range $[Q_2; Q_3]$, corresponding to a higher surface fractal dimension of $D_s \approx 2.9$, which reflects more irregular, highly rough surfaces with a greater degree of morphological complexity at the grain boundaries. This elevated surface roughness aligns closely with the properties of the CMK-3 additive itself. Specifically, the modified sample exhibits a surface scattering exponent ($\alpha \approx 3.1$) that closely approximates that of the pure CMK-3 reference ($\alpha \approx 3$), which corresponds to a surface fractal dimension approaching the theoretical upper limit of $D_s = 3$. This mutual similarity in surface morphology suggests a partial transfer of the additive's fractal surface characteristics to the composite. Such structural inheritance is plausible, given the high surface area and mesoporous nature of CMK-3, which can serve as a physical template or structural scaffold during the hydrogenation/dehydrogenation cycling. As hydride phases nucleate and grow within or adjacent to the CMK-3 matrix, the additive's rigid, ordered pore architecture may constrain particle growth, promoting interfacial roughness, and may prevent sintering or coarsening. Consequently, the composite retains the hierarchical, high-surface-area features of the carbon framework, leading to enhanced fractal surface morphology and improved accessibility for hydrogen sorption processes. These results confirm that, upon cycling, the CMK-3 additive promotes both smaller, less compact aggregate formation and enhanced surface roughness, contributing to a more porous and accessible microstructure for hydrogen sorption. To investigate the presence and stability of the CMK-3 mesoporous structure within the composite matrix, the scattering profile of the CMK-3 modified sample was reanalyzed using the Kratky representation and compared with that of the pristine CMK-3 reference material. As can be seen in Fig. 8b, within the characteristic scattering vector range $[Q_3; Q_4]$ associated with ordered mesopores, the modified sample does not have visible diffraction features attributable to CMK-3.

The particle size distributions, $N(r)*r^3$ *versus* radius r, derived from the modelling (eqn (13))[83] of scattering data for the BM samples are shown in Fig. S15b. The 6 : 9 : 2-RHC-BM
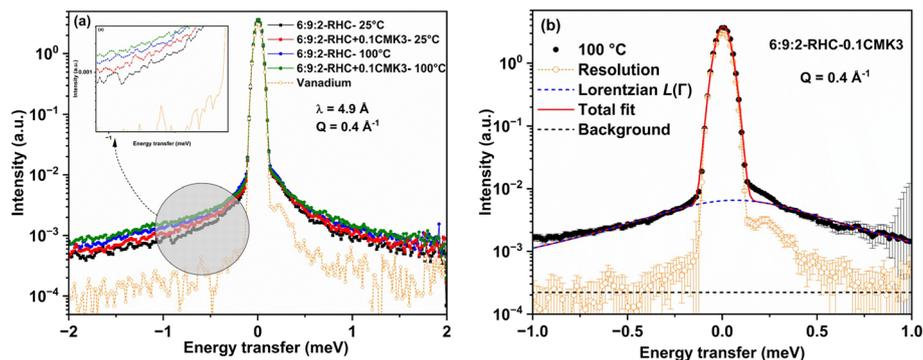
Fig. 9 Temperature-dependent QENS spectra of 6 : 9 : 2-RHC and 6 : 9 : 2-RHC + 0.1CMK3 (a) and QENS model fitting of 6 : 9 : 2-RHC + 0.1CMK3 (b) at a wavelength of 4.9 Å and Q of 0.4 Å^{-1}.

sample exhibits a broad distribution with a peak centered at approximately 5.5 μm. The addition of 10CMK3 results in a shift of the distribution for 6 : 9 : 2-RHC + 0.1CMK3-BM to smaller radii, with a peak at around 4.5 μm, and a slightly narrower overall distribution. Similarly, SI-Fig. S16e and f represent the particle size distribution after the first desorption cycle. The 6 : 9 : 2-RHC-des sample shows a broad distribution peaking around 4.5 μm. In contrast, the 6 : 9 : 2-RHC + 0.1CMK3-des sample displays a much sharper and narrower distribution, with its peak shifting significantly to smaller radii, approximately 3 μm.

$$I(q) = I_0\Big(\sin\big[(D-1)\arctan(Q\xi)\big]\Big/(D-1)Q\xi\big(1+Q^2\xi^2\big)^{(D-1)/2}\Big) \tag{13}$$

with:

$$\xi^2 = \frac{2R_g^2}{D(D+1)} \tag{13.1}$$

Here, D denotes the fractal dimension, and ξ corresponds to a characteristic linear size of the aggregate, which is proportional to the radius of gyration R_g.

The grain size distributions for the ball-milled samples show that both 6 : 9 : 2-RHC-BM and 6 : 9 : 2-RHC + 0.1CMK3-BM (SI-Fig. S16b and c) have distributions in the range of 15–20 nm. The distribution for 6 : 9 : 2-RHC + 0.1CMK3-BM appears slightly shifted to larger grain sizes and is somewhat broader than that of 6 : 9 : 2-RHC-BM. After the first desorption cycle, the grain size distributions are significantly altered. The 6 : 9 : 2-RHC-des sample shows a broad distribution peaking around 25–30 nm. Conversely, the 6 : 9 : 2-RHC + 0.1CMK3-des sample exhibits a much sharper and narrower grain size distribution, with its peak shifted to smaller sizes, approximately 17 nm. This suggests that CMK-3 helps to avoid particle agglomeration and enhance the diffusion or redistribution of components during hydrogen release. Structural characteristics of CMK-3 may enhance diffusion pathways for ionic species such as Li$^+$, H$^-$, NH$_2$$^-$, and BH$_4$$^-$, thus contributing to faster hydrogen release and improved kinetics. To confirm and further explore the ionic dynamics, QENS experiments were performed.

QENS experiments were performed on 6 : 9 : 2-RHC and 6 : 9 : 2-RHC + 0.1CMK3 in their desorbed state. In the desorbed state, the reaction products are Li$_4$(BH$_4$)(NH$_2$)$_3$, and Li$_2$Mg$_2$(NH)$_3$. QENS comprehensively investigates the ion dynamics (NH$_2$$^-$ and BH$_4$$^-$) and observes the effect of CMK-3 on these dynamics. QENS analyses were performed at neutron wavelengths of 4.9 Å and 8 Å. These wavelengths cover a momentum transfer (Q) range of 0.2 to 2.2 Å^{-1}, which is sufficient for the investigation of ion dynamics at multiple spatial and temporal scales. Measurements were performed across a temperature range of −73 °C to 200 °C to capture both low-temperature and high-temperature behaviors. For clarity, only data recorded at 25 °C and 100 °C are presented here (Fig. 9a), while analysis at additional temperatures is included in SI-Fig. S17.

To investigate the dynamical processes in the material, quasi-elastic neutron scattering (QENS) measurements were initially performed using a neutron wavelength of 4.9 Å. This wavelength provides access to higher momentum transfer (Q) values and is particularly sensitive to rapid, localized ionic motions. The QENS spectrum of 6 : 9 : 2-RHC at room temperature exhibits moderate broadening relative to elastic reference measured with vanadium, indicating the presence of dynamic processes within the sample (Fig. 9a, zoom-in). These dynamics are primarily attributed to reorientation and diffusive motions of ionic species, especially involving the [NH$_2$]$^-$ and [BH$_4$]$^-$ anions. In particular, the CMK3-containing sample (6 : 9 : 2-RHC + 0.1CMK3) shows more pronounced spectral broadening compared to 6 : 9 : 2-RHC, even at 25 °C (Fig. 9a). This suggests that the incorporation of mesoporous carbon enhances ionic mobility at lower temperatures. Furthermore, the QENS broadening increases with temperature, *e.g.*, at 100 °C, further supporting the role of CMK-3 in promoting faster ion dynamics. A detailed analysis aiming to decouple and characterize the individual contributions from [NH$_2$]$^-$ and [BH$_4$]$^-$ will be presented in a separate publication.

To analyze the type of motion and its geometry and to find the contribution of [BH$_4$]$^-$ and [NH$_2$]$^-$ dynamics, the experimental data of 6 : 9 : 2-RHC and 6 : 9 : 2-RHC + 0.1CMK3 have been fitted using eqn (14). It has a single Lorentzian function for quasielastic broadening, one resolution function derived from
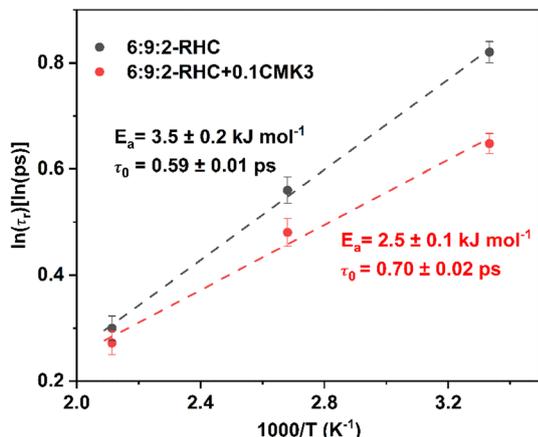
Fig. 10 Rotational activation energy and residence time of the pure system 6 : 9 : 2-RHC and with CMK-3.

vanadium standard for the elastic part and a flat background b_g to account for faster motions.[84]

$$S(Q,\omega) = R \otimes [A_0(Q)\delta(\omega) + A_1(Q)L(\Gamma)] + b_g \qquad (14)$$

Here, Γ is the HWHM of the Lorentzian function L, and A_0 and A_1 denote the elastic and quasielastic scattering intensities, respectively. The model fitting was performed at the data measured at 100 °C, shown in Fig. 9b and S18. Model fitting gives us critical information about the contribution of ion dynamics, HWHM, elastic contribution and quasielastic contribution, which can be used further to get useful information like geometry and type of motion.

The HWHM (Γ) of the Lorentzian function provides insight into the timescales of molecular motion for $[BH_4]^-$ and $[NH_2]^-$. It is directly related to the characteristic residence time (τ_r) of rotational movements through the relation $\Gamma \approx \hbar/\tau_r$, where $\hbar$ is the reduced Planck constant ($\hbar/2\pi$). As the temperature increases, molecular motion becomes faster, leading to broader Lorentzian peaks (higher Γ values), which indicate more frequent rotational jumps. The residence time (τ_r) between successive jumps is given by $\tau_r \approx \hbar/\Gamma$, which helps to determine the activation energy barrier for these thermally activated

motions. The rotational activation energy barrier for hydrogen-containing species $[BH_4]^-$ and $[NH_2]^-$ was calculated by fitting the relaxation time $\ln(\tau_r)$ and $1/T$ according to the Arrhenius equation (eqn (15)) to understand the impact of CMK-3 on reorientational energy barrier.

$$\tau_r = \tau_0 \exp(E_a/k_B T) \qquad (15)$$

The activation energy for the localized reorientations was calculated from the slope of the linear fit in Fig. 10. In the case of 6 : 9 : 2-RHC, the activation energy is 3.5 kJ mol^{-1}, indicating a moderate rotational energy barrier.[85] However, the addition of CMK-3 significantly reduced the rotational activation energy to 2.5 kJ mol^{-1}.

From the model fitting, using the perfectors A_0 and A_1, the elastic and quasielastic incoherent structure factors (EISF and QISF) were calculated using the following equations.

$$EISF = A_0/A_0 + A_1 \qquad (16)$$

$$QISF = A_1/A_0 + A_1 = 1 - EISF \qquad (17)$$

The measurements at room temperature yield an Elastic Incoherent Structure Factor (EISF) that is, on average, closer to unity compared to those obtained at higher temperatures. In general, an EISF value approaching one indicates that the atoms remain largely immobile within the time and length scales probed by the experiment. It suggests that a smaller fraction of BH_4^- anions undergo rotational motion at this temperature. The EISF value increases with temperature for both the pristine 6 : 9 : 2 and CMK-3 incorporated samples, indicating more active BH_4^- unit population. On the other hand, EISF values decrease with increasing Q for both the pristine 6 : 9 : 2-RHC and CMK-3 incorporated samples (Fig. 11a and b), which indicate the presence of localized motions with confined geometries.

To quantitatively estimate the fraction of dynamically inactive BH_4^- species (p), model fitting of the EISF data was performed using the selected rotational model. The EISF was compared with analytical expressions describing rotations of BH_4^- tetrahedra undergoing rapid uniaxial 120° around their C_2 and C_3 symmetry axes, given by eqn (18).[86]
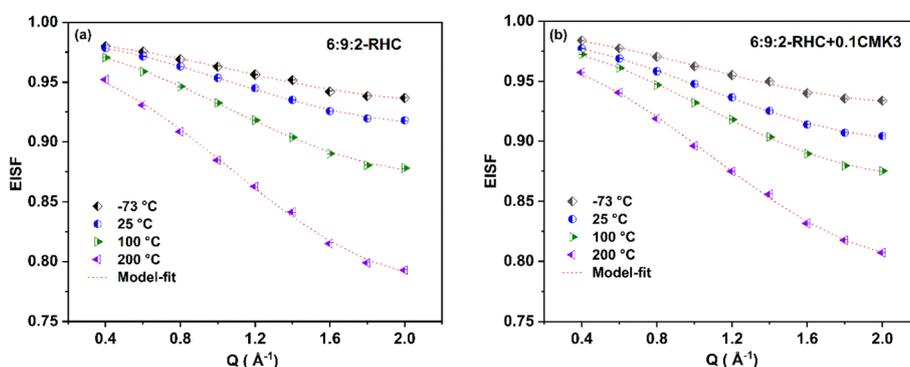

Fig. 11 EISF of 6 : 9 : 2-RHC (a) and EISF of 6 : 9 : 2-RHC + 0.1CMK3 (b).

$$A_{C_2/C_3} = \frac{1}{2}\left[1 + J_0\left(\frac{2\sqrt{2}}{\sqrt{3}}Qd_{B-H}\right)\right] \qquad (18)$$

Here, $j_0 = \dfrac{\sin(x)}{x}$ represents the zeroth-order spherical Bessel function, and d_{B-H} denotes the B–H bond distance. The fraction of hindered BH_4^- units is expressed by the parameter p, from which the $EISF_p$ and $QISF_p$ are defined. A simultaneous fit of $EISF_p$ and $QISF_p$ (Fig. 11a and b) with d_{B-H} varied between 1.12 and 1.22 Å.

$$EISF_p = s[p + (1-p)A_{C_2/C_3}] \qquad (19)$$

$$QISF_p = 1 - s[(p + (1-p)A_{C_2/C_3}] = 1 - EISF_p \qquad (20)$$

Model fitting of the QENS spectra indicates that the fraction of active BH_4^- species participating in the motion increases with temperature, increasing from ~10% at room temperature to ~30% at 200 °C in both the pristine and CMK-3 modified samples. The increase in the dynamically active fraction of BH_4^- ions correlates well with the QENS spectral broadening (FWHM) at elevated temperatures. The scale factor (s) accounts for small normalization differences between experimental data and the fitted model.

Furthermore, to understand the type of motion in $[BH_4]^-$ and $[NH_2]^-$ like localized or long-range, we studied the FWHM relation with Q. Both the materials show almost constant FWHM with increasing Q, a trend typical of localized dynamics rather than long-range diffusion (SI-Fig. S19).[70] Additionally, the FWHM broadening is more pronounced in the CMK-3 incorporated sample, suggesting that CMK-3 promotes faster dynamics, likely arising from the interface between its porous structure and the hydride phases. In SI-Fig. S20, data at 8 Å show minimal broadening, reinforcing the idea that CMK-3 primarily enhances dynamics at shorter length scales, corresponding to more localized motions.

4. Discussion

The incorporation of 10 wt% of CMK-3 into the reactive hydride composite $6Mg(NH_2)_2 + 9LiH + 2LiBH_4$ (6:9:2-RHC) shows significant improvement in the hydrogen absorption and desorption rates of the system, as demonstrated by the volumetric analysis (Fig. 3a). The CMK-3 modified sample was able to absorb its maximum hydrogen capacity within only 3 minutes, while the pristine system required around 30 minutes to reach full hydrogenation capacity. Similarly, the hydrogen desorption time decreased from 60 minutes in the pure hydride system to only 25 minutes in the CMK-3 modified sample, which represents a 58% reduction in the hydrogen desorption time. The volumetric analysis at low temperature (Fig. 3b) further confirms the catalytic role of CMK-3, as the hydrogen absorption/desorption time is also reduced compared to the pure system. Cycling stability tests (SI-Fig. 4) show that the CMK-3 modified sample maintains hydrogen capacity more effectively than the pure sample. After 10 dehydrogenation/hydrogenation cycles, the CMK-3 modified sample shows only 0.07 wt% capacity loss, compared to 0.12 wt% for the pristine

material. Using the DTA method (Fig. 2), we observed that the activation energy of the CMK-3 modified sample is reduced (106 ± 2 kJ mol⁻¹) compared to the pure system (117 ± 1 kJ mol⁻¹). Similarly, a range of carbon materials have been shown to enhance the reaction kinetics of metal hydrides in the literature.[87,88] In this work, the enhancement in hydrogen storage performance of the modified system could be correlated with structural and dynamical changes triggered by the addition of CMK-3. SANS/USANS measurements (Fig. 5–8) were carried out to monitor the structural changes from the milled state over the entire desorption/absorption cycle of the system. The SANS/USANS results of the milled samples show that CMK-3 modifies the hierarchical organization of the 6:9:2-RHC system across multiple length scales (Fig. 5 and 6). Both milled samples revealed a fractal structure over a large Q range in the USANS region. The CMK-3 modified composite exhibits a higher fractal exponent ($\alpha \approx 2.9$) compared to the pure sample ($\alpha \approx 2.3$), which reflects a more compact and connected network morphology closely resembling pristine CMK-3 ($\alpha \approx 3$). This indicates that the mesoporous carbon acts as a structural template, constraining particle agglomeration and preserving accessible surface area. Further results (Fig. 6 and 7) show that the mesostructural integrity of CMK-3 inside the modified sample is preserved after ball milling at both the micro- and nanoscales.

During ball milling, the presence of CMK-3 enables the 6:9:2-RHC system to reach a smaller mean particle size (~4.5 μm) compared to the pristine system (~5.5 μm) (SI-Fig. S15b). This reduction in mean size remains evident even after desorption, as the CMK-3 modified sample still exhibits a smaller mean particle size (SI-Fig. S15d). This confirms the role of CMK-3 in constraining particle agglomeration and preserving the accessible surface area. After a full dehydrogenation–hydrogenation cycle, the CMK-3 modified system maintains open mass fractal networks ($\alpha \approx 1.2$) with significantly enhanced surface roughness ($D_s \approx 2.9$), closely matching with the CMK-3 reference. This inheritance of fractal surface morphology promotes porous, highly irregular interfaces that may enhance hydrogen accessibility and diffusion through the phase boundaries. The pristine sample, in contrast, forms denser aggregates with smoother surfaces, potentially restricting hydrogen diffusion pathways. Although the amount of CMK-3 used is relatively small compared to the mass of the RHC, it provides a hierarchical structural framework that suppresses sintering, preserves nanostructural stability, and enhances surface roughness.

These structural effects underpin the enhanced hydrogen sorption kinetics by promoting smaller particle sizes, increased porosity, and shorter diffusion pathways, thereby accounting for the superior hydrogen storage performance of CMK-3 modified 6:9:2-RHC composites.

QENS analysis of 6:9:2-RHC and 6:9:2-RHC + 0.1CMK3 (Fig. 9a) demonstrates that the incorporation of CMK-3 significantly enhances the dynamics of $[BH_4]^-$ anions. At room temperature (25 °C), the CMK-3 modified sample shows noticeably stronger quasielastic broadening compared to pure 6:9:2-RHC, indicating that the presence of mesoporous carbon promotes faster hydrogen-containing anion dynamics

even under mild thermal conditions. At a higher temperature (100 °C), this effect becomes even more pronounced. The quasielastic broadening further increases, and the corresponding half-width at half-maximum (HWHM) (Fig. 9 a) values indicate faster molecular motion, translating into shorter residence times for rotational jumps. Model fitting of the $S(Q, \omega)$ spectra (Fig. 9b) confirms the distinct Lorentzian component, which represents the fast rotational motions of $[BH_4]^-$ anions. The calculated reorientational energy barrier decreases by ~30%, from 3.5 kJ mol^{-1} in the pristine 6 : 9 : 2-RHC sample to 2.5 kJ mol^{-1} in the CMK-3 modified composite (Fig. 10), which suggests that the presence of CMK-3 lowers the energy required for anion reorientation. This reduction in rotational energy barrier supports faster local reorientation of BH_4^-, which activates the B–H bond and facilitates local atomic rearrangements and increases the probability of interactions between the reactants.[89] The EISF data (Fig. 11) also exhibit a pronounced temperature dependence, which reflects the activation of localized reorientational motion of BH_4^- anions. Model fitting of the EISF confirmed that the fraction of dynamically active BH_4^- species increases from approximately 10% at room temperature to about 30% at 200 °C in both the pristine and CMK-3 modified samples, consistent with progressive thermal activation of BH_4^- reorientation. The Q-independent FWHM (SI-Fig. S19) of the quasielastic component demonstrates that the motions probed are localized rather than long-range diffusion,[90] suggesting that the carbon scaffold enhances dynamics primarily at interfaces between the hydride grains and the mesoporous framework.

These enhanced dynamics at both room and elevated temperatures directly correlate with improved hydrogen storage performance. These structural effects underpin the enhanced hydrogen sorption kinetics by promoting smaller grain sizes, increased porosity, and shorter diffusion pathways. The resulting faster dynamics statistically increase the likelihood that local interactions between reactants overcome kinetic barriers, ultimately leading to more efficient product formation. The CMK-3 additive therefore serves a dual role: (i) it provides a mesostructured scaffold that stabilizes smaller hydride grains and prevents agglomeration (as observed in SANS/USANS) and (ii) it promotes faster local dynamics of hydrogen-containing species, especially at room temperature where kinetic limitations are most critical. The kinetic model that better describe absorption and desorption (F1/F2) shows that the fundamental reaction pathways remain unchanged, as was confirmed by FT-IR and XRD analyses (Fig. 4 and S13),[9,10] while the overall kinetic rate is significantly improved.

5.   Conclusion

Through the combined use of cutting-edge experimental techniques, including volumetric measurements, DTA, SANS/USANS, QENS, FTIR and XRD, a comprehensive assessment of the effects of CMK-3 incorporation into the 6 : 9 : 2-RHC system has been carried out. The integration of the mesoporous carbon scaffold results in markedly faster hydrogen sorption kinetics, reduced desorption times, improved low-temperature performance and superior cycling stability compared to the pristine material. These improvements are underpinned by two key factors: (i) the structural role of CMK-3 in suppressing sintering, stabilizing smaller grains and preserving accessible surface areas across multiple length scales and (ii) the dynamic role of CMK-3 in facilitating faster reorientations of hydrogen-containing anions, thereby lowering activation barriers and promoting more efficient diffusion and reaction pathways. The experimental evidence demonstrates that even with relatively small amounts of CMK-3 incorporation, the composite exhibits hierarchical organization, enhanced surface roughness, and dynamic flexibility that collectively increase the probability of overcoming local kinetic barriers and forming hydrogenated or dehydrogenated products more efficiently. Importantly, CMK-3 strongly influences kinetics but it does not alter the fundamental reaction pathways or final dehydrogenation products, thus preserving the intrinsic reversibility of the 6 : 9 : 2-RHC system.

Overall, this work shows that the synergistic interplay between nanoscale structural stabilization and enhanced local molecular dynamics provides the mechanistic basis for the superior hydrogen storage performance of CMK-3 modified 6 : 9 : 2-RHC composites. This comprehensive, multi-technique approach highlights how careful assessment of structure–property relationships, enabled by advanced characterization methods, can reveal the fundamental reasons behind improved material functionality in hydrogen storage systems.

Author contributions

M. Abbas: conceptualization, methodology, validation, formal analysis, investigation, writing – original draft, visualization. F. Karimi: investigation, formal analysis, conceptualization, writing – review & editing. T. Le: writing – review & editing. J. Ollivier: review & editing, conceptualization, software. J. Mata: writing – review & editing, conceptualization, formal analysis, software. J. P. King: writing – review & editing, conceptualization, formal analysis. L. Vellingiri: formal analysis, review & editing. G. Stahlkopf: formal analysis, writing – review & editing. T. Klassen: resources, supervision, funding acquisition. C. Pistidda: supervision, conceptualization, resources, writing – review & editing, visualization, funding acquisition.

Conflicts of interest

The authors declare that they have no known competing financial interests or personal relationships that could have influenced the work reported in this paper.

Data availability

The data supporting the findings of this study are available from the corresponding author upon request.

Supplementary information (SI) is available. See DOI: https://doi.org/10.1039/d6ta00801a.

Acknowledgements

References

1 W. I. F. David, Effective hydrogen storage: a strategic chemistry challenge, *Faraday Discuss.*, 2011, **151**, 399–414.

2 M. Lavanya, S. Shrivastava, T. Lakshmi, E. R. Sandadi, S. Gour, N. A. Thomas, *et al.*, An overview of hydrogen storage technologies–Key challenges and opportunities, *Mater. Chem. Phys.*, 2024, 129710.

3 C. Pistidda, Solid-State Hydrogen Storage for a Decarbonized Society, *Hydrogen*, 2021, **2**(4), 428–443.

4 S.-i Orimo, Y. Nakamori, J. R. Eliseo, A. Züttel and C. M. Jensen, Complex hydrides for hydrogen storage, *Chem. Rev.*, 2007, **107**(10), 4111–4132.

5 T. He, H. Cao and P. Chen, Complex hydrides for energy storage, conversion, and utilization, *Adv. Mater.*, 2019, **31**(50), 1902757.

6 C. Milanese, T. Jensen, B. Hauback, C. Pistidda, M. Dornheim, H. Yang, *et al.*, Complex hydrides for energy storage, *Int. J. Hydrogen Energy*, 2019, **44**(15), 7860–7874.

7 C. Milanese, S. Garroni, F. Gennari, A. Marini, T. Klassen, M. Dornheim, *et al.*, Solid State Hydrogen Storage in Alanates and Alanate-Based Compounds: A Review, *Metals*, 2018, **8**(8), 567.

8 X. Yang, J. Kong, X. Lu, J. Su, Q. Hou and W. Li, Hydrogen storage properties of metal borohydrides and their improvements: Research progress and trends, *Int. J. Hydrogen Energy*, 2024, **60**, 308–323.

9 H. Cao, G. Wu, Y. Zhang, Z. Xiong, J. Qiu and P. Chen, Effective thermodynamic alteration to Mg(NH2)2–LiH system: achieving near ambient-temperature hydrogen storage, *J. Mater. Chem. A*, 2014, **2**(38), 15816–15822.

10 G. Gizer, J. Puszkiel, M. V. C. Riglos, C. Pistidda, J. M. Ramallo-López, M. Mizrahi, *et al.*, Improved kinetic behaviour of Mg(NH2)2-2LiH doped with nanostructured K-modified-LixTiyOz for hydrogen storage, *Sci. Rep.*, 2020, **10**(1), 8.

11 C. Jensen, Y. Wang and M. Y. Chou, 14 – Alanates as hydrogen storage materials, *Solid-State Hydrogen Storage*, ed. in Walker G., Woodhead Publishing, 2008, pp. 381–419.

12 G. L. Soloveichik, Metal borohydrides as hydrogen storage materials, *Mater. Matters*, 2007, **2**, 11–14.

13 J. Puszkiel, S. Garroni, C. Milanese, F. Gennari, T. Klassen, M. Dornheim, *et al.*, Tetrahydroborates: Development and Potential as Hydrogen Storage Medium, *Inorganics*, 2017, **5**(4), 74.

14 S. Garroni, A. Santoru, H. Cao, M. Dornheim, T. Klassen, C. Milanese, *et al.*, Recent Progress and New Perspectives on Metal Amide and Imide Systems for Solid-State Hydrogen Storage, *Energies*, 2018, **11**(5), 1027.

15 F. Karimi, S. Börries, P. K. Pranzas, O. Metz, A. Hoell, G. Gizer, *et al.*, Characterization of LiBH4–MgH2 reactive hydride composite system with scattering and imaging methods using neutron and synchrotron radiation, *Adv. Eng. Mater.*, 2021, **23**(11), 2100294.

16 F. Karimi, P. K. Pranzas, J. A. Puszkiel, M. V. C. Riglos, C. Milanese, U. Vainio, *et al.*, A comprehensive study on lithium-based reactive hydride composite (Li-RHC) as a reversible solid-state hydrogen storage system toward potential mobile applications, *RSC Adv.*, 2021, **11**(37), 23122–23135.

17 C. Milanese, T. R. Jensen, B. C. Hauback, C. Pistidda, M. Dornheim, H. Yang, *et al.*, Complex hydrides for energy storage, *Int. J. Hydrogen Energy*, 2019, **44**(15), 7860–7874.

18 R. Juza and K. Opp, Metallamide und metallnitride, 25. Mitteilung. zur kenntnis des lithiumimides, *Z. Anorg. Allg. Chem.*, 1951, **266**(6), 325–330.

19 P. Chen, Z. Xiong, J. Luo, J. Lin and K. L. Tan, Interaction of hydrogen with metal nitrides and imides, *Nature*, 2002, **420**(6913), 302–304.

20 Y. Nakamori, G. Kitahara and S. Orimo, Synthesis and dehydriding studies of Mg–N–H systems, *J. Power Sources*, 2004, **138**(1), 309–312.

21 H. Che, Y. Wu, X. Wang, H. Liu and M. Yan, Improved hydrogen storage properties of Li-Mg-N-H system by lithium vanadium oxides, *J. Alloys Compd.*, 2023, **931**, 167603.

22 H. Li, Z. Li, M. Luo, H. Yuan, Y. Wu, X. Guo, *et al.*, Review on Li–Mg–N–H-based lightweight hydrogen storage composites and its applications: challenges, progress and prospects, *J. Mater. Sci.*, 2023, **58**(42), 16269–16296.

23 S. Bhattacharya, G. Wu, C. Ping, Y. P. Feng and G. P. Das, Lithium Calcium Imide [Li2Ca(NH)2] for Hydrogen Storage: Structural and Thermodynamic Properties, *J. Phys. Chem. B*, 2008, **112**(36), 11381–11384.

24 Z. Xiong, G. Wu, J. Hu, Y. Liu, P. Chen, W. Luo, *et al.*, Reversible hydrogen storage by a Li–Al–N–H complex, *Adv. Funct. Mater.*, 2007, **17**(7), 1137–1142.

25 J. Lu, Z. Z. Fang, H. Y. Sohn, R. C. Bowman and S.-J. Hwang, Potential and Reaction Mechanism of Li−Mg−Al−N−H System for Reversible Hydrogen Storage, *J. Phys. Chem. C*, 2007, **111**(44), 16686–16692.

26 R. Janot, J.-B. Eymery and J.-M. Tarascon, Investigation of the processes for reversible hydrogen storage in the Li–Mg–N–H system, *J. Power Sources*, 2007, **164**(2), 496–502.

27 W. Luo, J. Wang, K. Stewart, M. Clift and K. Gross, Li–Mg–N–H: Recent investigations and development, *J. Alloys Compd.*, 2007, **446–447**, 336–341.

28 Z. Xiong, J. Hu, G. Wu, P. Chen, W. Luo, K. Gross, *et al.*, Thermodynamic and kinetic investigations of the hydrogen storage in the Li–Mg–N–H system, *J. Alloys Compd.*, 2005, **398**(1), 235–239.

29 C. Li, Y. Liu, R. Ma, X. Zhang, Y. Li, M. Gao, *et al.*, Superior Dehydrogenation/Hydrogenation Kinetics and Long-Term Cycling Performance of K and Rb Cocatalyzed Mg(NH2)2-2LiH system, *ACS Appl. Mater. Interfaces*, 2014, **6**(19), 17024–17033.

30 J. Wang, T. Liu, G. Wu, W. Li, Y. Liu, C. M. Araújo, *et al.*, Potassium-Modified Mg(NH2)2/2 LiH System for Hydrogen Storage, *Angew. Chem., Int. Ed.*, 2009, **48**(32), 5828–5832.

31 C. Li, Y. Liu, Y. Pang, Y. Gu, M. Gao and H. Pan, Compositional effects on the hydrogen storage properties of Mg(NH2)2–2LiH–xKH and the activity of KH during dehydrogenation reactions, *Dalton Trans.*, 2014, **43**(6), 2369–2377.

32 G. Gizer, F. Karimi, C. Pistidda, H. Cao, J. A. Puszkiel, Y. Shang, *et al.*, Effect of the particle size evolution on the hydrogen storage performance of KH doped Mg(NH2)2 + 2LiH, *J. Mater. Sci.*, 2022, **57**(22), 10028–10038.

33 L.-P. Ma, H.-B. Dai, Y. Liang, X.-D. Kang, Z.-Z. Fang, P.-J. Wang, *et al.*, Catalytically enhanced hydrogen storage properties of Mg (NH2) 2+ 2LiH material by graphite-supported Ru nanoparticles, *J. Phys. Chem. C*, 2008, **112**(46), 18280–18285.

34 T. Durojaiye, J. Hayes and A. Goudy, Rubidium Hydride: An Exceptional Dehydrogenation Catalyst for the Lithium Amide/Magnesium Hydride System, *J. Phys. Chem. C*, 2013, **117**(13), 6554–6560.

35 J. Wang, T. Liu, G. Wu, W. Li, Y. Liu, C. M. Araújo, *et al.*, Potassium-modified Mg (NH2) 2/2 LiH system for hydrogen storage, *Angew. Chem., Int. Ed. Engl.*, 2009, **48**(32), 5828–5832.

36 G. Amica, S. Enzo, P. A. Larochette and F. C. Gennari, Improvements in the hydrogen storage properties of the Mg(NH2)2–LiH composite by KOH addition, *Phys. Chem. Chem. Phys.*, 2018, **20**(22), 15358–15367.

37 F. Torre, A. Valentoni, C. Milanese, C. Pistidda, A. Marini, M. Dornheim, *et al.*, Kinetic improvement on the CaH2-catalyzed Mg(NH2)2+2LiH system, *J. Alloys Compd.*, 2015, **645**, S284–S287.

38 J. Hu, Y. Liu, G. Wu, Z. Xiong, Y. S. Chua and P. Chen, Improvement of hydrogen storage properties of the Li–Mg–N–H system by addition of LiBH4, *Chem. Mater.*, 2008, **20**(13), 4398–4402.

39 J. Hu, M. Fichtner and P. Chen, Investigation on the Properties of the Mixture Consisting of Mg(NH2)2, LiH, and LiBH4 as a Hydrogen Storage Material, *Chem. Mater.*, 2008, **20**(22), 7089–7094.

40 H. Wang, H. Cao, G. Wu, T. He and P. Chen, The improved Hydrogen Storage Performances of the Multi-Component Composite: 2Mg(NH2)2–3LiH–LiBH4, *Energies*, 2015, **8**(7), 6898–6909.

41 J. J. Vajo, T. T. Salguero, A. F. Gross, S. L. Skeith and G. L. Olson, Thermodynamic destabilization and reaction kinetics in light metal hydride systems, *J. Alloys Compd.*, 2007, **446–447**, 409–414.

42 J. Yang, A. Sudik, D. J. Siegel, D. Halliday, A. Drews, R. O. Carter 3rd, *et al.*, A self-catalyzing hydrogen-storage material, *Angew. Chem., Int. Ed. Engl.*, 2008, **47**(5), 882–887.

43 G. Gizer, J. Puszkiel, H. Cao, C. Pistidda, T. T. Le, M. Dornheim, *et al.*, Tuning the reaction mechanism and hydrogenation/dehydrogenation properties of 6Mg(NH2) 29LiH system by adding LiBH4, *Int. J. Hydrogen Energy*, 2019, **44**(23), 11920–11929.

44 H. Wang, G. Wu, H. Cao, C. Pistidda, A.-L. Chaudhary, S. Garroni, *et al.*, Near Ambient Condition Hydrogen Storage in a Synergized Tricomponent Hydride System, *Adv. Energy Mater.*, 2017, **7**, 1602456.

45 A. Bhatnagar, S. K. Pandey, V. Dixit, V. Shukla, R. R. Shahi, M. A. Shaz, *et al.*, Catalytic effect of carbon nanostructures on the hydrogen storage properties of MgH2–NaAlH4 composite, *Int. J. Hydrogen Energy*, 2014, **39**(26), 14240–14246.

46 P. A. Berseth, A. G. Harter, R. Zidan, A. Blomqvist, C. M. Araújo, R. H. Scheicher, *et al.*, Carbon Nanomaterials as Catalysts for Hydrogen Uptake and Release in NaAlH4, *Nano Lett.*, 2009, **9**(4), 1501–1505.

47 M. A. Lillo-Ródenas, Z. X. Guo, K. F. Aguey-Zinsou, D. Cazorla-Amorós and A. Linares-Solano, Effects of different carbon materials on MgH2 decomposition, *Carbon*, 2008, **46**(1), 126–137.

48 H. Cheng, L. Xu, X. Fan, X. Huang, J. Liu, K. Yan, *et al.*, Synergistic effects played by CMK-3 and NbF5 co-additives on de/re-hydrogenation performances of NaAlH4, *Int. J. Hydrogen Energy*, 2018, **43**(20), 9705–9712.

49 R. Balu, N. R. Choudhury, J. P. Mata, L. de Campo, C. Rehm, A. J. Hill, *et al.*, Evolution of the Interfacial Structure of a Catalyst Ink with the Quality of the Dispersing Solvent: A Contrast Variation Small-Angle and Ultrasmall-Angle Neutron Scattering Investigation, *ACS Appl. Mater. Interfaces*, 2019, **11**(10), 9934–9946.

50 K. Wood, J. P. Mata, C. J. Garvey, C.-M. Wu, W. A. Hamilton, P. Abbeywick, *et al.*, QUOKKA, the pinhole small-angle neutron scattering instrument at the OPAL Research Reactor, Australia: design, performance, operation and scientific highlightsThis article will form part of a virtual special issue on advanced neutron scattering instrumentation, marking the 50th anniversary of the journal, *J. Appl. Crystallogr.*, 2018, **51**(2), 294–314.

51 E. A. Cheung, H. Nguyen, M. Avdeev, N. R. de Souza, Y. S. Meng and N. Sharma, Insights into the Fast Sodium Conductor NASICON and the Effects of Mg2+ Doping on Na+ Conductivity, *Chem. Mater.*, 2021, **33**(22), 8768–8774.

52 M. B. Amdisen, Y. Cheng, N. Jalarvo, D. Pajerowski, C. M. Brown, T. R. Jensen, *et al.*, The Influence of

Reorientational and Vibrational Dynamics on the Mg2+ Conductivity in Mg(BH4)2·CH3NH2, *Chem. Mater.*, 2024, **36**(19), 9784–9792.

53 K. Sköld, Quasielastic neutron scattering studies of metal hydrides, in *Hydrogen in Metals I: Basic Properties*, ed. G. Alefeld and J. Völkl, Berlin, Heidelberg, Springer Berlin Heidelberg, 1978, pp. 267–287.

54 G. Gizer, *Role of Additives on the Kinetic and Thermodynamic Properties of Mg (NH₂)²⁺ LiH Reactive Hydride Composite*, PhD thesis, Helmut-Schmidt-Universität/Universität der Bundeswehr Hamburg, 2020.

55 H. E. Kissinger, Reaction kinetics in differential thermal analysis, *Anal. Chem.*, 1957, **29**(11), 1702–1706.

56 J. H. Sharp, G. W. Brindley and B. N. N. Achar, Numerical data for some commonly used solid state reaction equations, *J. Am. Ceram. Soc.*, 1966, **49**(7), 379–382.

57 L. F. Jones, D. Dollimore and T. Nicklin, Comparison of experimental kinetic decomposition data with master data using a linear plot method, *Thermochim. Acta*, 1975, **13**(2), 240–245.

58 J. A. Puszkiel, *Tailoring the Kinetic Behavior of Hydride Forming Materials for Hydrogen Storage, Gold Nanoparticles-Reaching New Heights*, 2018.

59 N. Schell, R. Martins, F. Beckmann, H. Ruhnau, R. Kiehn and A. Schreyer, The High Energy Materials Science Beamline at PETRA III, *Mater. Sci. Forum*, 2008, **571–572**, 261–266.

60 A. Hammersley, *FIT2D: An Introduction and Overview*, 1997.

61 A. L. Patterson, The Scherrer formula for X-ray particle size determination, *Phys. Rev.*, 1939, **56**(10), 978.

62 K. Wood, J. P. Mata, C. J. Garvey, C.-M. Wu, W. A. Hamilton, P. Abbeywick, *et al.*, QUOKKA, the pinhole small-angle neutron scattering instrument at the OPAL Research Reactor, Australia: design, performance, operation and scientific highlights, *Appl. Crystallogr.*, 2018, **51**(2), 294–314.

63 C. Rehm, Ld Campo, A. Brûlé, F. Darmann, F. Bartsch and A. Berry, Design and performance of the variable-wavelength Bonse–Hart ultra-small-angle neutron scattering diffractometer KOOKABURRA at ANSTO, *Appl. Crystallogr.*, 2018, **51**(1), 1–8.

64 L. Barré, Contribution of Small-Angle X-Ray and Neutron Scattering (SAXS and SANS) to the Characterization of Natural Nanomaterials, in *X-Ray and Neutron Techniques for Nanomaterials Characterization*, ed. C. S. S. R. Kumar, Berlin, Heidelberg, Springer Berlin Heidelberg, 2016, pp. 665–716.

65 S. R. Kline, Reduction and analysis of SANS and USANS data using IGOR Pro, *Appl. Crystallogr.*, 2006, **39**(6), 895–900.

66 M. Gavrilov, E. P. Gilbert, A. E. Rowan, J. Lauko and G. E. Yakubov, Structural Insights into the Mechanism of Heat-Set Gel Formation of Polyisocyanopeptide Polymers, *Macromol. Rapid Commun.*, 2020, **41**(18), 2000304.

67 S. Kline, Reduction and analysis of SANS and USANS data using IGOR Pro, *J. Appl. Crystallogr.*, 2006, **39**(6), 895–900.

68 J. Kohlbrecher and I. Breßler, Updates in SASfit for fitting analytical expressions and numerical models to small-angle scattering patterns, *Appl. Crystallogr.*, 2022, **55**(6), 1677–1688.

69 J. A. Crake-Merani, *SasView Version 6.1.1. Zenodo*, 2025.

70 M. Kruteva, Dynamics studied by Quasielastic Neutron Scattering (QENS), *Adsorption*, 2021, **27**(5), 875–889.

71 M. T. F. Telling, *A Practical Guide to Quasi-Elastic Neutron Scattering*, Royal Society of Chemistry, 2020.

72 J. Ollivier and H. Mutka, IN5 Cold Neutron Time-of-Flight Spectrometer, Prepared to Tackle Single Crystal Spectroscopy, *J. Phys. Soc. Jpn.*, 2011, **80**, SB003.

73 M. Abbas, M. Appel, Karimi, A. Kuznetsova, T. T. Le, J. Ollivier, C. Pistidda and M. Ramond, *Quasi Elastic Neutron Scattering (QENS) Study of 6Mg(NH2)2-9KH-xLiBH4 with Inorganic Additives (Graphene, CMK-3) as Solid State Electrolyte*, Institut Laue-Langevin (ILL), 2023, DOI: 10.5291/ILL-DATA.7-03-231.

74 O. Arnold, J. C. Bilheux, J. M. Borreguero, A. Buts, S. I. Campbell and L. Chapon, *et al.*, Mantid—Data analysis and visualization package for neutron scattering and μ SR experiments, *Nuclear Instruments and Methods in Physics Research Section A: Accelerators, Spectrometers, Detectors and Associated Equipment*, 2014, vol. 764, pp. 156–166.

75 R. T. Azuah, L. R. Kneller, Y. Qiu, P. L. W. Tregenna-Piggott, C. M. Brown, J. R. D. Copley, *et al.*, DAVE: a comprehensive software suite for the reduction, visualization, and analysis of low energy neutron spectroscopic data, *J. Res. Natl. Inst. Stand. Technol.*, 2009, **114**(6), 341.

76 J. Hu, E. Weidner, M. Hoelzel and M. Fichtner, Functions of LiBH 4 in the hydrogen sorption reactions of the 2LiH–Mg (NH 2) 2 system, *Dalton Trans.*, 2010, **39**(38), 9100–9107.

77 S.-J. Huang, Y. Y. Tanoto, M. P. Mose and C. Li, Exploring the impact of the ball milling process on the homogenous blending of polyamide 6-AZ61 magnesium powders, *Powder Technol.*, 2025, **452**, 120527.

78 J. Kohlbrecher, *SASfit: A Program for Fitting Simple Structural Models to Small Angle Scattering Data*, 2009.

79 E. Anitas, *Small-Angle Scattering from Mass and Surface Fractals*, 2018.

80 B. Hammouda, A new Guinier-Porod model, *J. Appl. Crystallogr.*, 2010, **43**(4), 716–719.

81 E. Walenta, O. G. Von and O. Kratky, Small angle x-ray scattering, London, Academic Press Inc. Ltd 1982. ISBN 0-12-286280-5. X, 515 Seiten, geb. £ 43,60; US $ 81.00, *Acta Polym.*, 1985, **36**(5), 296.

82 K. L. Stefanopoulos, C. Tampaxis, A. A. Sapalidis, F. K. Katsaros, T. G. Youngs, D. T. Bowron, *et al.*, Total neutron scattering study of supercooled CO2 confined in an ordered mesoporous carbon, *Carbon*, 2020, **167**, 296–306.

83 C. M. Sorensen, J. Cai and N. Lu, Test of static structure factors for describing light scattering from fractal soot aggregates, *Langmuir*, 1992, **8**(8), 2064–2069.

84 M. Bée, Localized and long-range diffusion in condensed matter: state of the art of QENS studies and future prospects, *Chem. Phys.*, 2003, **292**(2–3), 121–141.

85 J. B. Grinderslev, U. Häussermann, T. R. Jensen, A. Faraone, M. Nagao, M. Karlsson, *et al.*, Reorientational Dynamics in Y

(BH4) 3· *x* NH3 (*x*= 0, 3, and 7): The Impact of NH3 on BH4–Dynamics, *J. Phys. Chem. C*, 2024, **128**(11), 4431–4439.

86 T. Burankova, L. Duchêne, Z. Łodziana, B. Frick, Y. Yan, R.-S. Kühnel, *et al.*, Reorientational Hydrogen Dynamics in Complex Hydrides with Enhanced Li+ Conduction, *J. Phys. Chem. C*, 2017, **121**(33), 17693–17702.

87 D. Pukazhselvan, B. K. Gupta, A. Srivastava and O. N. Srivastava, Investigations on hydrogen storage behavior of CNT doped NaAlH4, *J. Alloys Compd.*, 2005, **403**(1), 312–317.

88 P. Adelhelm and P. E. De Jongh, The impact of carbon materials on the hydrogen storage properties of light metal hydrides, *J. Mater. Chem.*, 2011, **21**(8), 2417–2427.

89 A. Remhof, P. Mauron, A. Züttel, J. P. Embs, Z. Łodziana, A. J. Ramirez-Cuesta, *et al.*, Hydrogen Dynamics in Nanoconfined Lithiumborohydride, *J. Phys. Chem. C*, 2013, **117**(8), 3789–3798.

90 R. Lavén, U. Häussermann, A. Perrichon, M. S. Andersson, M. S. Targama, F. Demmel, *et al.*, Diffusional Dynamics of Hydride Ions in the Layered Oxyhydride SrVO2H, *Chem. Mater.*, 2021, **33**(8), 2967–2975.